PURDUE UNIVERSITY
GRADUATE SCHOOL
Thesis/Dissertation Acceptance

This is to certify that the thesis/dissertation prepared

By Timothy James Sego

Entitled
FINITE ELEMENT ANALYSIS OF AND MULTISCALE SKELETAL TISSUE MECHANICS CONCERNING A SINGLE DENTAL IMPLANT SITE

For the degree of Master of Science in Mechanical Engineering

Is approved by the final examining committee:

Andres Tovar
Chair

Tien-Min G. Chu

Sohel Anwar

To the best of my knowledge and as understood by the student in the Thesis/Dissertation Agreement, Publication Delay, and Certification Disclaimer (Graduate School Form 32), this thesis/dissertation adheres to the provisions of Purdue University's "Policy of Integrity in Research" and the use of copyright material.

Approved by Major Professor(s): Andres Tovar

Approved by: Sohel Anwar 4/20/2016
Head of the Departmental Graduate Program Date

FINITE ELEMENT ANALYSIS OF AND MULTISCALE SKELETAL TISSUE MECHANICS CONCERNING A SINGLE DENTAL IMPLANT SITE

A Thesis

Submitted to the Faculty

of

Purdue University

by

Timothy James Sego

In Partial Fulfillment of the

Requirements for the Degree

of

Master of Science in Mechanical Engineering

May 2016

Purdue University

Indianapolis, Indiana

To those giants who rose before me, upon whose shoulders I may now stand.

ACKNOWLEDGMENTS

I would like to thank my advisers, Professors Andrés Tovar and Tien-Min Gabriel Chu, for their guidance, support and trust throughout the completion of this work, as well as Professor Yung-Ting Hsu, with whom I have had the pleasure of co-authoring my first academic contribution. The year that is conveyed in the succeeding pages has been one of the most significant eras of both my personal and professional lives, for which I will always be grateful. In retrospect, it is plainly clear to me that, having discovered a sincere desire to explore the unknown, I am all only better because of it.

I would like to thank the Purdue University Department of Mechanical Engineering and the Indiana University School of Dentistry, for the financial means to pursue this work during the past year, without which only a fraction of the potentially useful information presented might have been pursued.

I would like to thank Carli, who was there.

Finally, I would like to thank my family and friends, who over the past year have quietly missed me and patiently endured my perpetual droning on about strains, singularities and what interesting things bones do. Sadly, I cannot present this work as a sincere gesture of my renewed sociality.

PREFACE: AN INFORMAL NOTE TO THE READER

This work is intended for those with a professional or personal interest in the topics and applications associated with the biomechanical aspects of oral implants. I, the author, readily admit that, on the chance that any expert from some involved field find their way to this work, at least some degree of mercy on the part of the expert reader is probably required, since only a year ago I was entirely ignorant of what all bone does. My own understanding of the requisite biological concepts was largely constructed from the works of Dr. David B. Burr and Dr. R. Bruce Martin, whose collective published works are, in my opinion, more than sufficient to appreciate any advanced literature on skeletal mechanobiology. In all transparency, the majority of my knowledge on these topics, which is summarized in Chapter 1 as relevant to the succeeding work and in the fewest possible words, originates from their first edition of Skeletal Tissue Mechanics (which was with Dr. Neil A. Sharkey).

The work here originates from the collaborative research of Drs. Andés Tovar and Tien-Min Gabriel Chu, who through their mutual biomechanical interests have patiently and mercifully advised me. It was through them that I was introduced to Dr. Yung-Ting Elizabeth Hsu, and with our respective backgrounds we all set ourselves to enhance the versatility of the clinician's repertoire. Chapter 4 documents my contribution to our work, which is supported by Chapters 2 and 3. Chapter 5 documents my attempt to extend the usefulness of our modeling description of bone, based on some of the limitations that I observed during the work, which I hope, in the least, provokes some better mind to produce something useful. Chapters 2 through 4 are written as interdependent studies, each with its own unique introduction, which (hopefully) conveys the progression of the work in an honest form.

T.J.S.

TABLE OF CONTENTS

Page

LIST OF TABLES

LIST OF FIGURES

Figure Page

SYMBOLS

d_{ij}	damage tensor
f	plastic flow potential
h_{ij}	remodeling tensor
$\hat{h}_{ij}$	fabric tensor
$\tilde{h}_{ij}$	remodeling tensor in material coordinate system
n	porosity
s_{ij}	deviatoric stress tensor
t	time
u	Heaviside step function
$\dot{v}$	unit volume rate
A^{ε}	strain sensitivity
B	material law coefficient
C_{ijkl}	elasticity tensor
$\tilde{C}_{ijkl}$	elasticity tensor in material coordinate system
D	scalar damage
D^{L}	accumulated loading scalar damage
D^{mech}	mechanical damage
E	elastic Young's modulus
$\hat{E}$	undamaged Young's modulus
F	softening law
H	principal remodeling value
I	first material axis
II	second material axis
III	third material axis
N^{c}	density of resorption cavities

N^H	density of Haversian canals
N^r	density of resorbed trabeculae
N^T	density of trabeculae
P	load component
R^c	radius of a resorption cavity
R^H	radius of a Haversian canal
R^T	radius of a trabecula
T	period
V	control volume
V^m	mass volume
V^v	void volume

Greek symbols

β	material law power coefficient
δ_{ij}	second-order Kronecker-delta
ϵ_{ijk}	Levi-Civita symbol
ε_{ij}	total strain tensor
ζ	mean resorption volume of a trabecula
ζ^r	mean volume of a trabecula at full resorption
ζ^T	mean volume of a trabecula before resorption
η	mean volume of a resorption cavity
η^c	mean volume of a resorption cavity at full resorption
η^H	mean volume of a Haversian canal
λ	plastic multiplier
ν	Poisson's ratio
ρ	bone density
ρ^H	Haversian threshold density
$\hat{\rho}$	ideal bone density
σ_{ij}	Cauchy stress tensor
χ_i	remodeling process dependents

Superscripts

o	initial
f	formation
pl	plastic
r	resorption
re	reduced effective
C	cortical
D	damaged
H	Haversian
T	trabecular
U	ultimate
UD	undamaged
Y	yield

Subscripts

x	first global axis
y	second global axis
z	third global axis

ABBREVIATIONS

BH	bilinear hardening
BMU	basic multicellular unit
cc	cubic centimeter
CAD	computer-aided design
CH	crown height
C/I	crown-to-implant
CT	computed tomography
DOE	design of experiments
FE	finite element
FEA	finite element analysis
FEM	finite element method
IL	implant length
PEA	photoelastic analysis
SD	standard deviation

ABSTRACT

Sego, Timothy James. M.S.M.E., Purdue University, May 2016. Finite Element Analysis of and Multiscale Skeletal Tissue Mechanics Concerning a Single Dental Implant Site. Major Professors: Andrés Tovar and Tien-Min Gabriel Chu.

Finite element analysis (FEA) in implantology is performed in design applications concerning the complex topology of an implant, according to theoretical assumptions about and clinical data concerning the biomechanical nature of skeletal tissue. Implants are placed in topologically and physiologically complex sites, and major disagreement exists in literature about various aspects concerning their modeling and analysis. Current research seeks to improve the implementation of an implant by the use of short implants, which negate the necessity of additional surgical procedures in regions of limited bone height. However, short implants with large crown heights introduce biomechanical complications associated with increased stress and strain distributions in skeletal tissue, which may cause bone loss and implant failure. The short implant is characterized by the geometric ratio of the crown height to the implant length, called the crown-to-implant (C/I) ratio.

In this work nonlinear FEA was performed to investigate the effects and significance of the C/I ratio on long-term implant stability. A finite element model was developed according to literature, and emulation of previous research and comparison of reported results were performed. Comparison of results demonstrated significant sources of error in previous research, which are argued to be caused by mesh-dependency from common model idealizations in literature. A convergence test was then performed, which verified the mesh-dependency of results and challenged the reliability of some common model assumptions and methods of analysis in literature. A 16-point design of experiments was then performed to evaluate the significance and influence of the C/I ratio, considering a proposed novel method for evaluating

results and predicting long-term stability. Analysis of results demonstrated that the C/I ratio augments the inherent biomechanical effects of an implant design, particularly overloading strain concentrations at implant interface features. The use of short implants with high C/I ratios is determined to be inadvisable, considering the physiological response of tissue to strain distributions and biological context. A novel, multiscale material model is then proposed to describe the short-term accumulation of damage and biomechanical remodeling response in orthotropic skeletal tissue, as a potential solution to the mesh-dependency of results.

1. INTRODUCTION

1.1 Multiscale Description of Bone

Bone is an organic, dynamic, porous structure that serves a number of functional purposes [1]. Bone minerals contribute to approximately 7.8% of the weight of the human body [2], and are organized into two different types of bone, called *cortical* and *trabecular* bone. Macroscopically, each type of bone is characterized by porosity and directionality, with corresponding mechanical descriptions. Consequentially, bone can be mechanically described as a dynamic, anisotropic material. Cortical bone, also known as compact bone, provides the primary structural function of bone, is 5-10% porous and is typically found as a cortex of relatively consistent directionality and surrounding trabecular bone. Trabecular bone, also called cancellous bone, is 75-95% porous, can vary greatly in directionality and is filled with *marrow*, which serves a number of biochemical functions [3]. The mechanical properties of both bone types have been extensively studied, though much disagreement exists among results, neglecting the significant variation between anatomical regions, species and subjects, and the differences between *in vivo* and *ex vivo*.

In topologically simple regions (for example, a long bone) the distinct microstructure (50-1,000 μm) of each type of bone is apparent. Mineral in trabecular bone is arranged as a complex matrix of interconnected struts, called *trabeculae*, of approximately 200 μm thickness. The matrix of the trabecular system occupies the inner volume of the cortical shell. Cortical bone consists of a Haversian system of partially and fully formed fibers, called *osteons*, with an approximate diameter of 200 μm. Partially formed osteons are overlapped by those of full form, which have at their fiber axis a non-mineralized volume called a *Haversian canal* of approximately 50 μm diameter. The Haversian system has access features, called *Volkmann's canals*,

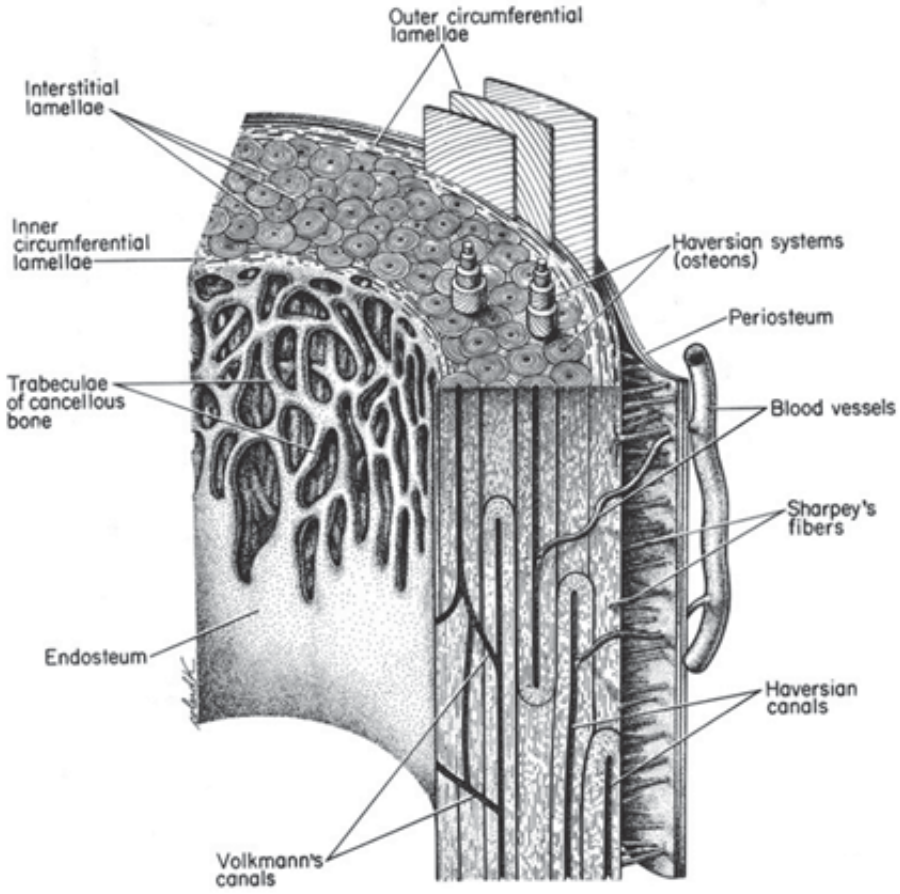

Figure 1.1. Sketch of some important features of a typical long bone. Reproduced from [1] with permission from Springer.

through which blood vessels and possibly nerves penetrate the cortical shell and occupy Haversian canals. The Haversian system also includes *resorption cavities*, which are non-mineralized volumes where osteons are being formed and, at their largest, have an approximately 200 μm diameter (Figure 1.1).

1.2 Structural Adaptation and Skeletal Tissue Mechanics

Bone is known to adapt to biomechanical conditions [4]. In the biological paradigm of evolutionary advantage, the hypothesis that organisms adapt to changes in living conditions [5] is supported by biomechanical observations that the trajectory of tra-

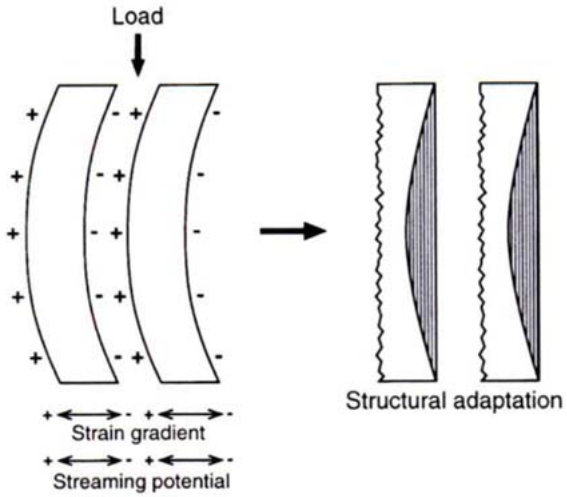

Figure 1.2. Bending is associated with stress (and strain) gradients. If the polarity of these gradients is as defined in the text, then they would have + and - signs as shown in the longitudinal section at *left*. The streaming potentials produced by these stress gradients would have simliar polarity. If positive and negative signals produce resoprtion and formation, respectively, the bone would straighten as shown in the *right* diagram. Reproduced from [1] with permission from Springer.

becular systems tend to align with principal stress directions [6]. The hypothesis is further supported by observations of the effects of an osteotomy on overloading strains and bone growth in bovine [7], bone loss in canines from prolonged disuse [8], and many other observed phenomena [9]. These mechanophysiological phenomena, combined with the consequences of evolutionary pressures associated with body weight and skeletal strength, are collectively referred to as *Wolff's Law*. In the words of Wolff himself, the structural adaptation of skeletal tissue has to do with "form and function" [10]: bone restructures to better serve the functions required for a repeated mechanical stress state, while using the least amount of material possible. The processes of structural adaptation are observed to occur in two modes. The first mode, called *modeling*, is the resorption and formation of bone tissue in macroscopically distinct regions (Figure 1.2). The second is referred to as *remodeling*, where resorption and formation in the macroscale occur in the same region.

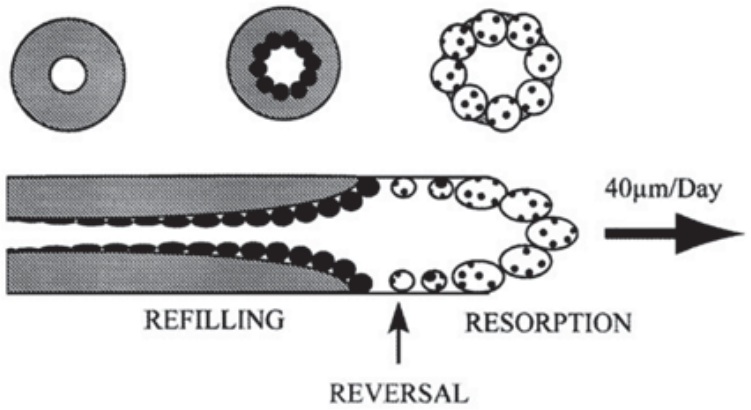

Figure 1.3. Schematic diagram of an osteonal BMU. Larger, multinucleated cells to *right* are osteoclasts; smaller cells shown in *black* to *left* are osteoblasts. Cross-sectional views are shown *above*. Not to scale. Reproduced from [1] with permission from Springer.

In the microscale, bone resorption is accomplished by the *osteoclast*, and formation is performed by the *osteoblast*, which deposits *osteoid* that mineralizes into bone tissue. Groups of these two cells collect together to form the *basic multicellular unit* (BMU), which accomplishes remodeling processes. In the Haversian system, each osteon is the byproduct of the remodeling processes performed by a BMU (Figure 1.3). Resorption cavities are the current work of some nearby BMU, the progressing resorption surface of which is the *cutting cone*. In the trabecular system, the BMU travels along the surface of and digs into trabeculae. The exact mechanisms by which bone senses and responds to mechanical stress states are currently unknown.

1.3 FEA and Implantology

Finite element analysis (FEA) is the virtual modeling and analysis of a system by means of the finite element method (FEM). In structural FEM, a geometry is partitioned into discrete volumes, called elements, the solutions of which are formulated and simultaneously solved for a given problem statement. FEA is most commonly implemented when studying complex geometries, for which no feasible analytical so-

lution can be formulated. FEA has been used to study various aspects of implant design and stability since 1976 [11], and has become more advanced, to the incorporation of peripheral technologies like computed tomography (CT), the modeling of microstructures [12] and the simulation of theoretical descriptions of structural adaptation [13].

Concerning the study of implant design, a common application of FEA in implantology is the continuum model [14–23]. For the purpose of computational efficiency, the continuum model assumes the idealization that skeletal tissue can be modeled as uniformly continuous. This idealization is also frequently extended to assuming isotropic material properties of both types of bone, as well as linear elasticity and a neglect of plastic deformation. Implant design analyses typically consider the long-term scenario in which an implant has fully bonded to cortical and trabecular tissues, a condition called *osseointegration*. Under these model assumptions, various loads and physical scenarios are simulated and analyzed, for the purpose of studying various factors associated with bone loss and implant failure. Maximum results in one or both bone tissues are often reported, and spatial results distributions are analyzed. Given the significant disagreement concerning the experimental mechanical properties of bone tissue, the array of potential model assumptions and the technical details of any given finite element (FE) model, conclusions from finite element analyses using the continuum model may vary greatly.

1.4 Knowledge Gap

One common design parameter of current research is the crown-to-implant (C/I) ratio [20, 22–24], which is the ratio of the exposed length of an implant assembly to the osseointegrated implant length. The C/I ratio is of particular interest to clinicians in application to regions of limited bone height, where smaller implant lengths for a given crown height may be utilized to avoid more costly surgery. Clinically, implant design recommendations state that an acceptable crown height can be no greater than

an implant length [25], while one retrospective study suggests that, with the inclusion of splinted implants, higher C/I ratios cause less crestal bone loss [26]. Furthermore, some clinical data suggests that the C/I ratio has no influence on crestal bone loss [27]. Data has also suggested and been corroborated by experimental work that long-term stability can be expected from crown heights less than 15 mm, regardless of C/I ratio [24].

Still, given the usefulness and clinical success of the short implant [28], the continuum FE model continues to be utilized in the study of implant design. Work using FEA [20,23] and photoelastic analysis (PEA) [24,29] have both shown a positive correlation between the C/I ratio and stress distribution and maximum results, and that stress concentrations are significantly affected by lateral force. However, previous implant design studies using FEA demonstrated significant disagreement about the magnitude and distribution of results [20, 23]. Disagreement about reported results distributions was most apparent near sharp corners and the implant interface with cortical bone, which are bonded and dissimilar in material properties. Both sharp corners and bonded, dissimilar materials are known to produce singular configurations and significant model errors [30, 31]. These regions of disagreement about results are of clinical interest, since they have been observed to experience significant crestal bone loss *in vivo* [32]. Disagreements among FE models of the implant site include the degree of mesh detail [33,34], the consideration of trabecular architecture [12,35–37], material modeling of skeletal tissue [11] and analyzed maximum results [21, 23, 35]. Many studies assumed an isotropic model of skeletal tissue, which significantly affects results distributions and maximum results [38–40]. Concerning uncertainty about the implications of model results, implant stability has been proposed to be associated with implant interface surface area [33] and predicted by quantifying volumetric regions of overloaded tissue [18].

1.5 Research Objectives

The work in the succeeding chapters is concerned with the aforementioned biomechanical aspects of a single dental implant site. The work utilizes a continuum FE model of a soft-tissue implant in a simplified crestal ridge. The research objectives of this work are (1) to determine the limitations of the typical implant FE model; (2) to propose novel enhancements to implant modeling, including (i) a method of analysis of the biomechanical functional response of skeletal tissue to loading; and (ii) a material model to describe the accumulation of and biomechanical response to plastic deformation from a single load case; and (3) to determine the effects and significance of the crown-to-implant ratio on the long-term stability of a single dental implant, considering the predicted biomechanical response to loading. The hypothesis of this work is that, by augmenting the biomechanical effects of the strain concentrations in skeletal tissue from an implant design, increasing C/I ratios may associate with greater overloading in bone.

2. A PROPOSED FE MODEL OF AN IMPLANT SITE AND ITS COMPARISON TO PREVIOUS WORKS

2.1 Introduction

FEA has become increasingly useful for the study of implants [11]. This is largely because of the limitations of experimental methods *in vivo* and biological relevance of circumstances *ex vitro*, prompting researchers to explore analytical and numerical experimentation. Because of the highly complex geometry of an implant assembly (that is, the implant, abutment and assembly components), analytical descriptions are, at best, unmanageable, making FEA the primary resource among *in silico* methods. While a great deal of clinical data in implantology is retrospective, FEA has been utilized to model and predict phenomena that have been significantly unobservable *in situ*, including loading during interface development [41], structural adaptation [42,43] and responses to insertion torque [34].

A large amount of research has been performed using FEA to study the effects of various factors in the design of implants [44] like implant thread features [16,18], neck design [21] and length [15, 20, 23]. Still broader works have used FEA to better understand the interactions of neighboring implants by proximity [14] and mastication with the position of foodstuff [40]. Many researchers have studied various aspects of isolated implant sites under static loading [45], where in typical FE models skeletal tissue is modeled as continuous, linearly elastic and isotropic, and the implant interface is modeled as bonded with bone under the assumption of perfect osseointegration. These have prompted investigations of FE models using FEA to better understand the influence of such assumptions by comparing results using isotropic and anisotropic material properties [39] and different frictional descriptions of the implant interface [12].

Still, there is a lack of consensus about certain details of the implant FE model. One such disagreement among studies is the material description of biological tissue [11]. This is likely because research is still investigating a precise mechanical description of bone [46–50], given the potential for the consistency of bone to vary widely by site and patient [51]. Another disagreement is the results of interest, whether principal [12] or deviatoric [15], whether stress, micromotion [21] or damage [18]. Accordingly, in this work an FE model is proposed that was developed according to various details reported in literature. FE models from collected literature are emulated using nonlinear static structural analysis, the results of which are then compared to those reported in literature for validation and insight into the lack of consensus in literature.

2.2 Materials and Methods

2.2.1 Description of Model

A three-dimensional parametric CAD model of an implant assembly placed in a crestal ridge was generated using Creo Parametric v. 2.0 (PTC, Massachusetts, USA). The model was developed under the assumptions of continuous tissue of both bones, perfect osseointegration of the implant and perfect implant integration. The model of cortical bone consisted of an outer layer of uniform thickness enclosing an inner core of trabecular bone. The crestal ridge was modeled with a horizontal, planar superior surface (width of 6 mm). Consistently with previous studies, round and chamfer features were not added to cortical bone along the implant interface at the superior face of the ridge. The implant model was developed from the specifications of a popular soft-tissue implant (Straumann Institute, Waldenburg, Switzerland) of standard size (diameter of 4.1 mm). To avoid complications during meshing, virtual topology was applied at erroneous edge and face artifacts that were generated from revolved features. Within the scope of the study, the abutment and crown were modeled as a simple, cylindrical extrusion, henceforth called the load post, which

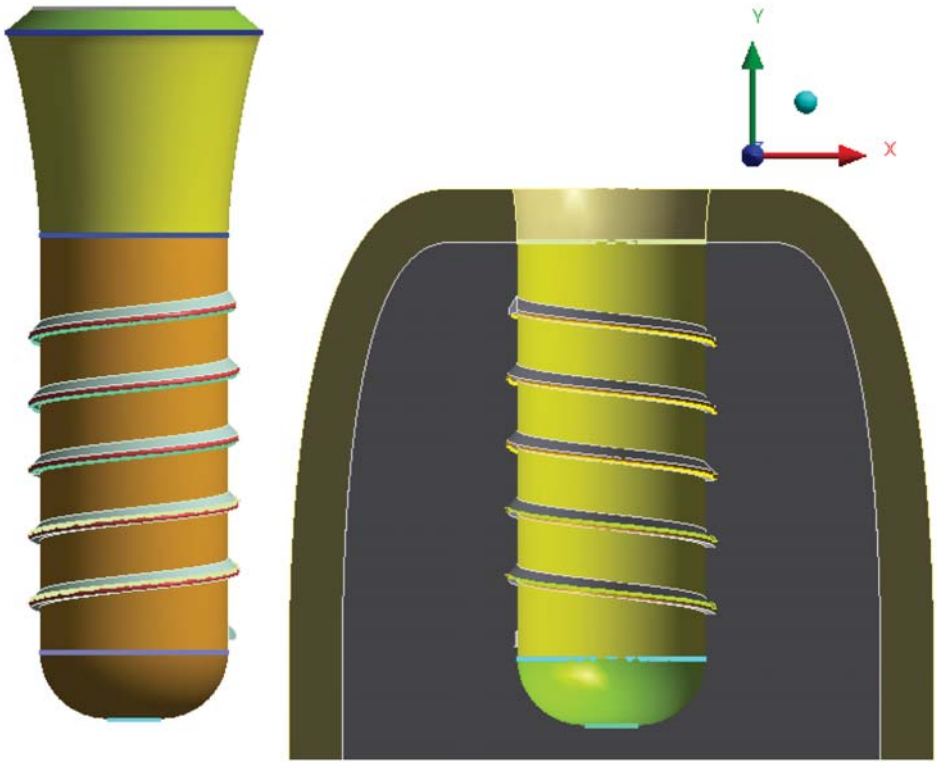

Figure 2.1. CAD model and virtual topology of the implant and crestal ridge (IL = 10 mm).

was extruded from the superior face of the implant. To increase the efficiency of simulations, simplifications were made to the implant by removing features that were outside of the scope of the study. The neglected features consisted of all internal connectivity to an abutment. (Figure 2.1).

The model was parameterized according to relevant dimensions during analysis of an implant. The model parameters include: (1) the crown height CH, measured from the superior surface of the crestal ridge to the loading surface of the load post; (2) the implant length IL, calculated as the total implant assembly length minus the crown height; (3) the uniform thickness of the cortical shell τ, (4) the material properties of both skeletal tissues; and (5) both load components P_x and P_y applied to the loading surface of the load post. For this study, lateral loading was appiled in

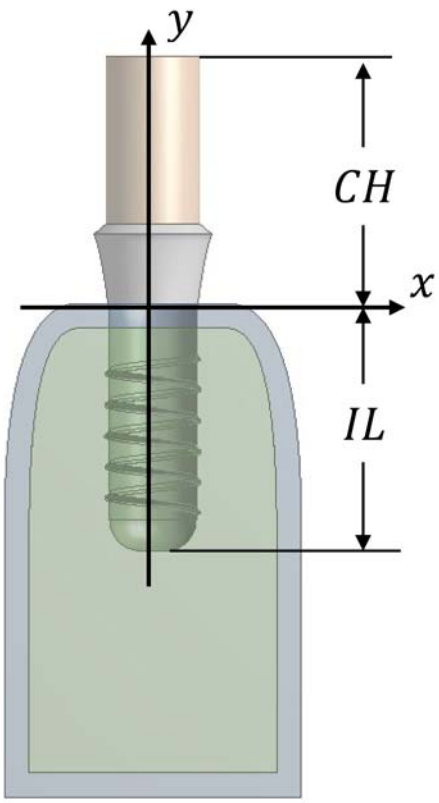

Figure 2.2. Considered geometric parameters of the implant site.

the buccal-lingual plane, which for the model orientation was the $x-y$ plane (Figure 2.2).

Considering these model parameters and conditions, four previous studies were collected that studied similar implant sites and that provided sufficient (or nearly sufficient) information for comparison and verification of the model [14, 22, 23, 39]. Each study was replicated by determining the corresponding model parameters of this study (geometric, material and loading) and by assuming any necessary parameter that was not explicitly reported; at least one assumption was required by every study except one (Table 2.1). The designated model parameters of each study were applied to the model configuration to determine which studies, if any, the model best supports.

The parameterized geometric model was then imported into the FEA software ANSYS v.15 (ANSYS, Inc., Pennsylvania, USA). Model parameters from collected

Table 2.1. Model parameters from collected literature.

Trial	CH (mm)	IL (mm)	τ (mm)	P_x (N)	P_y (N)	Source	Source model notes
1	10.0	10.0	1.0	0	-200	[22]	0° angulation
2	10.0	10.0	1.0	100	0	[22]	
3	5.0	10.0	2.0	40	-200	[39]	
4	10.0	8.5	1.0	0	-200	[23]	
5	12.5	8.5	1.0	0	-200	[23]	
6	15.0	8.5	1.0	0	-200	[23]	
7	10.5	8.5	1.0	100	0	[23]	
8	12.5	8.5	1.0	100	0	[23]	
9	15.0	8.5	1.0	100	0	[23]	
10	3.0	7.0	2.0	0	-70	[14]	
11	3.0	7.0	2.0	30.3	-17.5	[14]	2 cm implant distance
12	3.0	7.0	2.0	14	0	[14]	

literature were recorded, to emulate the various reported model configurations. Nonlinear FEA under static loading was applied to all configurations. Loading was directly applied to the superior face of the extruded load post, and fixed boundary conditions were applied to both tissues and at the extreme vertical surfaces of the site (that is, the mesial and distal boundaries). All contacts were modeled as bonded to fulfill the assumption of perfect osseointegration (Figure 2.3).

2.2.2 Mesh Details

Quadratic hexahedral elements were globally assigned to cortical bone. The mesh was mapped to the interface of cortical bone with the implant, inflated radially and sized to divide the cortical shell thickness into three equal element layers. The perime-

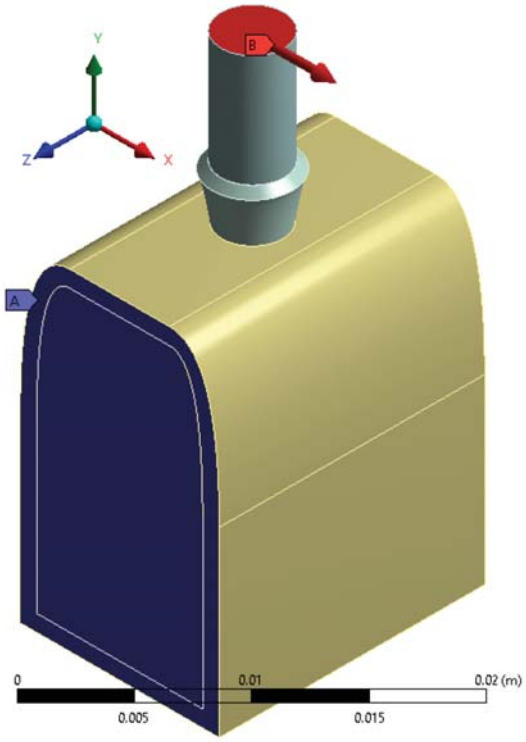

Figure 2.3. Proposed FE model setup.

ter of the interface at the superior and inferior faces of the cortical shell were then uniformly divided. The perimeter divisions, radially inflated initial length and inflation growth rate of the contact elements were programmed such that all contact elements had an aspect ratio of approximately 1 (38 divisions, 660 μm inflated length, 0.25 growth rate). The number of inflated layers was then set equal to two, for sufficient clearance to generate appropriately sized elements as the mesh transitioned into free form. Quadratic tetrahedral elements were assigned to the implant and programmed about the interface with cortical bone, with 80 evenly spaced divisions (Figure 2.4).

In trabecular bone, quadratic tetrahedral elements were globally assigned. The mesh was mapped to the implant interface, at the surface of the outer diameter of the thread feature, and sized to place two elements along the surface path (90 μm element size). To accurately capture contact interactions at the cylindrical features of

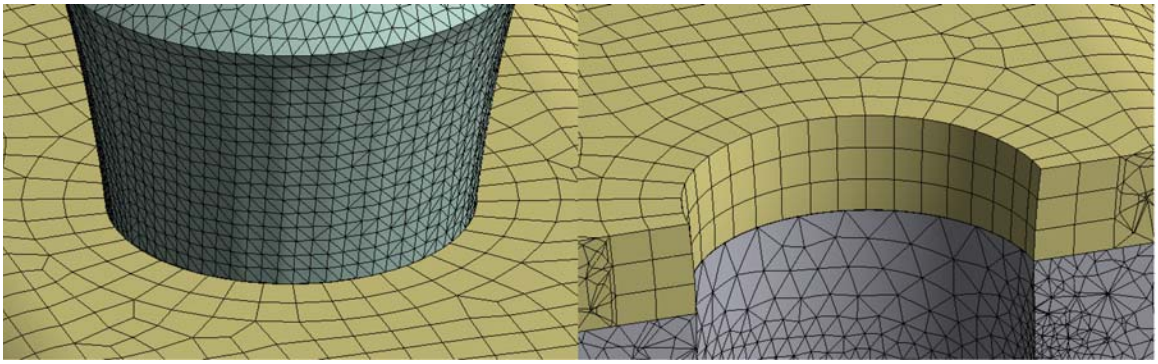

Figure 2.4. Detailed view of the mesh at the implant interface with cortical bone.

the implant interface, the mesh was programmed with a slow transition rate (Figure 2.5).

The mesh was designed using a test configuration of IL = 10 mm (Table 2.2). After verifying that no observable sources of significant error were present in the test model, project files were generated for all implant lengths from collected literature.

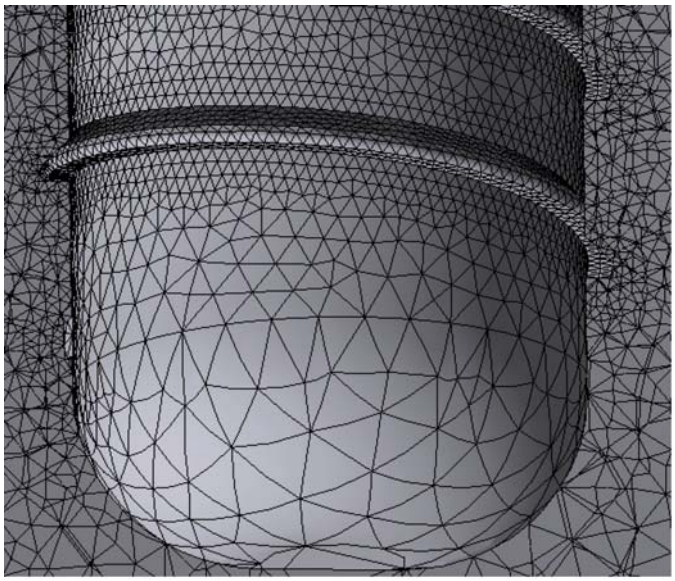

Figure 2.5. Detailed view of the mesh at the inferior surface of the implant interface with trabecular bone

Table 2.2. Mesh statistics of the FE model for a 10 mm implant length.

Part	Number of Nodes	Number of Elements
Implant (excluding load post)	304,499	208,224
Cortical bone	186,943	119,370
Trabecular bone	509,881	358,800
Total	1,001,323	686,394

The crown height, loading components and material properties were parameterized per collected study of interest. To ensure that no unanticipated errors occurred during parameterization, the project files for each implant length were manually reconstructed and individually verified by inspection. FEA was performed on a personal computer, Intel i7-4790k (4.00 GHz) processor, 16.0 GB RAM.

2.2.3 Material Properties

Several previous studies have shown that the assumption of isotropic material properties in bone significantly influences resulting stress and strain values [38–40]. Despite this, all collected literature but one [39] only modeled cortical and trabecular bone as isotropic. To remain consistent with collected literature, both skeletal tissues were modeled as isotropic, and material properties were taken directly from literature (Table 2.3). To fulfill the assumption of perfect implant integration, no variations in material properties were modeled in the neighborhood of the implant. The heterogeneity of trabecular bone was neglected for the purpose of simplification, though the neglect of individual trabeculae may introduce significant errors in modeling of the implant interface [37]. The implant and load post were modeled as isotropic according to a titanium alloy Ti6Al4V used in dental implants: Young's Modulus of 110 GPa, Poisson's ratio of 0.35.

Table 2.3. Material properties for cortical and trabecular bone in the literature comparison.

Young's Modulus (GPa)		Poisson's ratio		Source
Cortical	*Trabecular*	*Cortical*	*Trabecular*	
13.70	1.370	0.30	0.30	[22]
16.50	0.482	0.34	0.26	[39]
13.70	1.370	0.30	0.30	[23]
14.80	1.850	0.30	0.30	[14]

2.3 Results

Collected literature cited various results of interest, whether a principal stresses and/or strains in either or both tissues. For comparison, this study considered applicable results of the model per selected study. Tables 2.4 through 2.7 show the comparison of the model results with the collected literature results according to the maximum stress σ and microstrain $\mu\varepsilon$, the first (tension) and third (compression) principal results 1 and 3, respectively, and in cortical C and trabecular T tissues. For each result of each source, a percent error and population standard deviation of error (SD) were calculated to better understand the agreement between the source and the model without regard to the scale of the result. The individual results for each source were then averaged for comparison between the sources. The percent error was calculated according to the formula

$$\%Error = \frac{MR - LR}{LR} \cdot 100\%$$

where MR and LR are the model result and literature result, respectively.

Table 2.4 shows the results of the two trials that were conducted while comparing the first principal stress results in cortical bone (σ_1^C) to those reported in literature [22]. The applied load was varied from axial to lateral while holding all other parameters constant, the results of which from both the literature and pro-

Table 2.4. Maximum results from the literature comparison for trials 1 and 2.

Trial	Literature Results	Model Results	% Error
	σ_1^C	σ_1^C	σ_1^C
1	-1	17.76	-1876
2	27.02	154.42	471
	% Mean Error		-702
	±SD		±1174

posed model demonstrated a positive correlation between the loading angle of attack and maximum first principal stress in cortical bone. However, the results of the proposed model were significantly greater than those from literature and for Trial 1 was of opposite sign, with a mean error and standard deviation of -702±1,174%.

Table 2.5 shows the results of the trial that was conducted while comparing the first and third principal microstrain values in cortical and trabecular bone ($\mu\varepsilon_1^C$, $\mu\varepsilon_3^C$, $\mu\varepsilon_1^T$ and $\mu\varepsilon_3^T$, respectively) to those reported in literature [39] for each of two neighboring implants. The implants in literature were individually loaded and spaced sufficiently far to demonstrate no significant interaction. The results of the proposed model were lesser in cortical bone and greater in trabecular bone than those from literature, and the most supportive of any collected literature, with mean errors and standard deviations between -25±11% (for $\mu\varepsilon_1^C$) and 84±15% (for $\mu\varepsilon_3^T$).

Table 2.6 shows the results of the trials that were conducted while comparing the maximum first principal stress and microstrain results in cortical bone (σ_1^C and $\mu\varepsilon_1^C$, respectively) to those reported in literature [23]. The crown height was varied for purely axial and lateral load cases while holding all other parameters constant. Results from literature and the proposed model demonstrated a positive correlation between crown height and both results of interest under lateral loading. Contrarily, results from literature also indicated effects of the crown height on both results of interest under axial loading, while results from the proposed model demonstrated

Table 2.5. Maximum results from the literature comparison for trial 3.

Trial	Literature Results				Model Results			
	$\mu\varepsilon_1^C$	$\mu\varepsilon_3^C$	$\mu\varepsilon_1^T$	$\mu\varepsilon_3^T$	$\mu\varepsilon_1^C$	$\mu\varepsilon_3^C$	$\mu\varepsilon_1^T$	$\mu\varepsilon_3^T$
3	2655	-4454	4115	-3710	1692	-3062	6448	-7374
	1974	-4044	5167	-4379				
					% Error			
3					-36	-31	57	99
					-14	-24	25	68
	% Mean Error				-25	-28	41	84
	±SD				±11	±3	±16	±15

Table 2.6. Maximum results from the literature comparison for trials 4 through 9.

Trial	Literature Results		Model Results		% Error	
	σ_1^C	$\mu\varepsilon_1^C$	σ_1^C	$\mu\varepsilon_1^C$	σ_1^C	$\mu\varepsilon_1^C$
4	-0.19	116.4	16.54	1022	-8803	778
5	-0.23	131.3	16.55	1024	-7297	680
6	-0.28	147.4	16.57	1025	-6017	596
7	2.29	395.8	109.92	6778	4700	1613
8	3.25	566.9	134.84	8322	4049	1368
9	3.40	712.5	161.82	10016	4659	1306
	% Mean Error				-1451	1057
	±SD				±5979	±387

Table 2.7. Maximum results from the literature comparison for trials 10 through 12.

Trial	Literature Results				Model Results			
	σ_1^C	σ_3^C	σ_1^T	σ_3^T	σ_1^C	σ_3^C	σ_1^T	σ_3^T
10	3.7	-3.6	0.76	-0.59	5.49	-9.55	1.86	-2.54
11	11.1	-19.7	2.15	-1.40	10.73	-15.54	1.46	-1.55
12	4.1	-5.0	0.25	-0.27	6.05	-6.07	0.46	-0.52
					% Error			
10					48	165	144	331
11					-3	-21	-32	10
12					48	21	82	94
	% Mean Error				31	55	65	145
	±SD				±24	±80	±73	±136

no correlation whatsoever. Literature reported negative values for maximum first principal stress under axial loading, which contributed significant variation in the comparison of results to the proposed model. Results from the proposed model were significantly greater in magnitude for both results of interest and least supportive of any literature comparison, with a mean error and standard deviation of -1,451±5,979% in cortical bone stress and 1,057±387% in trabecular bone.

Table 2.7 shows the results of the trials that were conducted while comparing the maximum first and third principal stresses in cortical and trabecular bone (σ_1^C, σ_3^C, σ_1^T and σ_3^T, respectively) to literature [14]. The load was varied from axial to lateral over three trials, with a magnitude of 70, 35 and 14 N and angle of application with the implant axis of 0°, 60° and 90°, while holding all other parameters constant. Literature reported positive values for extreme third principal stresses. Because of the apparent agreement of results, those positive values were assumed to mean the largest magnitude of compressive stress, which were then compared to results from the

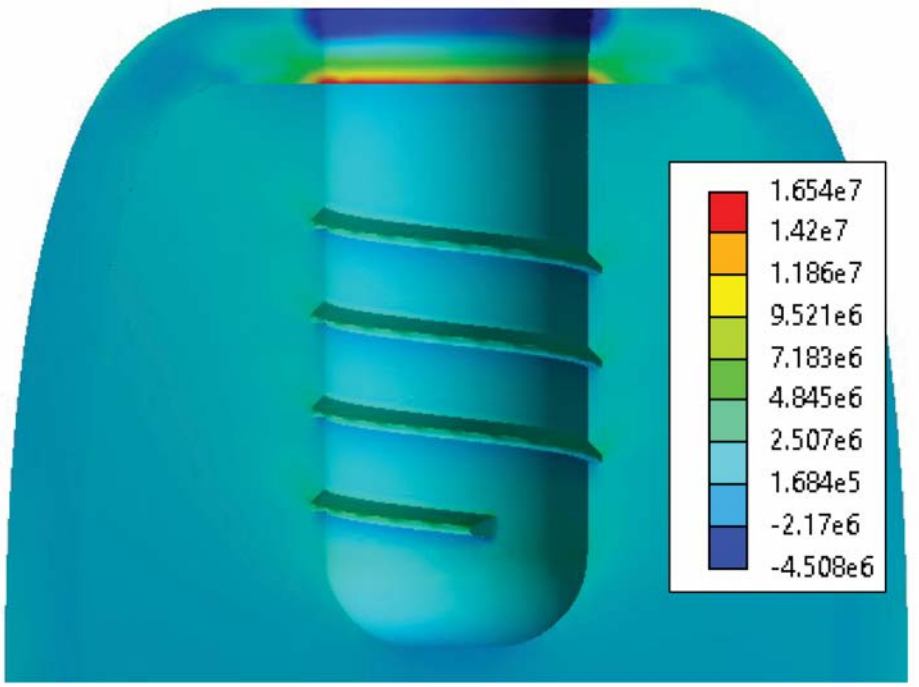

Figure 2.6. Results sample of the literature comparison for the trial with the most disagreement with collected literature (Trial 4, 1st principal stress)

proposed model as negative values. Results from the proposed model were mostly greater in magnitude than those from literature, with as much of a mean error as 55±80% in cortical bone and 145±136% in trabecular bone.

Figure 2.6 shows a sample of results from the literature comparison for trial 4. For all trials, results demonstrated significant concentrations of stress and strain in cortical bone at the superior and inferior perimeters of the implant interface, and in trabecular bone at the thread features of the implant interface. In both tissues, the stress and strain distributions generally emanated in a continuous manner from these features, as well as from the inferior face of the implant interface in trabecular bone. Relatively higher degrees of results were also observed in trabecular bone at the superior interface with cortical bone.

2.4 Discussion

Of immediate interest is the excessive degree of discrepancy between results from the proposed model and those from some literature, while other comparisons demonstrated more acceptable disagreement. Disregarding the disagreement about the sign of certain reported maximum results (Tables 2.4 and 2.6), the disagreement of the magnitude of results with certain literature is of particular concern. Though the most comparable results in cortical and trabecular bone were at best 3% and 10% (Table 2.7), the presence of significant sources of error is demonstrated by that disagreement with multiple sources for multiple trials was in excess of 1000%.

Review of reported model details did indicate some potential explanations for what might have contributed to such widely varying agreement between collected literature and the proposed model. Those studies in relative agreement with the proposed model did implement an implant with a similarly course thread pitch to the one used in the proposed model, while those studies in major disagreement used an implant of a finer thread. The difference in thread pitch does not, however, explain disagreement about results in cortical bone, neither does literature support this explanation for such large disagreement about results in trabecular bone [16]. Models in major disagreement implemented a full prosthetic assembly including an abutment, retaining screw and crown, while models of relative agreement implemented simplified models similarly to the proposed model. As an explanation for disagreement about results in cortical and trabecular bone, this difference in modeling features is inconsistent with St. Venant's Principle.

The remaining observed differences between collected literature and the proposed model were the implemented mesh and consistency of results distributions. From what information is reported in collected literature, those studies in major disagreement with the proposed model implemented a notably finer mesh for cortical bone than those studies in relative agreement. This potential correlation may explain the agreement about results for cortical bone, though in the proposed model trabecular

bone was also simulated with a fine mesh. Little to no information is reported in collected literature about mesh details in trabecular bone. However, differences between the proposed model and collected literature about the general consistency of results distributions in cortical provides some insight by deduction.

Applied numerical methods to stress analysis like the traditional finite element method are known to have limitations that arise from the approximations that are implemented in their formulation. Specifically to the typical implant FE model, complications arise when applying the traditional FEM to regions with edges and sharp corners [30]. The details of these complications are largely outside of the scope of the present work, but what is relevant is the potential propagation of errors throughout a model without the mitigation of these complications. In the proposed implant model and in those from collected literature, sharp corners exist at the implant interface with both cortical and trabecular bone. With the presence of non-negligible model errors, results distributions would be incomparable to solutions to similar problems, where little to no qualitative similarity can be determined. This is further complicated by both the material dissimilarity between the implant and both skeletal tissues, and by the potential existence of a free-edge singularity in cortical bone [31]. While neither approximation errors nor singularities can be used to reasonably argue for the validity of the proposed model or any of those from collected literature *per se*, what can be concluded, at the very least, is that the notable qualitative and quantitative disagreements about results warrant good reason to suspect a significant degree of mesh-dependency in results from the typical implant FE model.

3. ON THE EFFECTS OF MESH REFINEMENT AT THE IMPLANT INTERFACE

3.1 Introduction

Analysis of results in Chapter 2 demonstrated the likelihood of at least some significant degree of mesh-dependency in the results of typical implant FE models. This was deduced from significant disagreement about various results of interest in skeletal tissue for similar FE models and emulated assumptions, material properties and boundary conditions. Those differences included the magnitude of extreme principal stresses and strains in skeletal tissue, as well as the quality of their distributions in the neighborhood of the implant interface. While dissimilarities in geometric minutia may explain disagreement about results to some extent, results showed quantitative differences on the order of a thousand percent.

The limitations of FEA in orthopedic biomechanics have been explored in literature [52]. A great deal of work has been performed in the recent past to improve the accuracy of *in silico* methods, which have been described as requiring rigorous validation [37]. Given the highly complex consistency of bone and the difficulty of correlating experimental work with *in vivo* material descriptions, research has been performed to study the influence of anisotropy in numerical models [39,40] and anisotropic yielding [53]. The modeling of the highly complex geometry of a trabecular system has been accomplished using microscale CAD models from patient-specific μCT data of mandibles [12,35,36,54], and its influence on results compared to continuum modeling was investigated [37]. A major drawback to implementing most of these progresses is the enormous addition of required resources, whether computational or technological. This augmented barrier of entry may seriously inhibit research on implant design in the near future. The relatively reasonable computational and technological costs of

continuum modeling of biomaterials is exploited in FE-applied design methodologies. To study the influence of design factors that are well beyond any feasible analytical description, DOE methodology is often employed with statistical methods. Designs and design features are compared by simulation in the same model setup and circumstance. Advanced design methods like topology optimization have been utilized with FEA to reduce implant volume without significant reductions in biomechanical performance [19], and even the implementation cellular automata algorithms as a potential description for the structural adaptation of bone [13].

Between research in improving the accuracy of FE models and the applications of FEA in implant design, a conundrum occurs about the compromise of effectiveness and efficiency; that is, between the physical relevance of the continuum model and its accessibility. In application to the study of an implant site, a convergence test was performed on a typical continuum FE model considering isotropic, linear elastic material properties and plastic hardening post-yield behavior in skeletal tissue, to better understand what significant sources of error may be present, and to validate and improve the proposed model presented in Chapter 2.

3.2 Materials and Methods

A version of the FE model described in Chapter 2 was exported and modified to perform a convergence test of a typical implant model. The exported configuration included the parameterized CAD model, fixed boundary conditions, loading surface and bonded contacts. The experimental implant configuration was based on the test configuration during development of the mesh (implant length of 10 mm, crown height of 10 mm). A cortical shell thickness of 1.0 mm and a moderate lateral load (50 N) at the loading surface of the load post were assigned to the model (Table 3.1).

To observe the maximum results of both principal stresses and strains, the maximum von-Mises stress and total equivalent strain were recorded for all trials of the convergence test. Results were only recorded in cortical bone, since (1) results in

Table 3.1. Model parameters from the convergence test.

Model parameter	Symbol	Value
Crown height	CH	10 mm
Implant length	IL	10 mm
Cortical thickness	τ	1.0 mm
Lateral load component	P_x	50 N
Axial load component	P_y	0

Chapter 2 were more consistent in cortical bone; and (2) the implant interface with cortical bone is more clearly similar to a singular configuration described in [55]. Aside from recording maximum results, samples of results at the implant interface with cortical bone were taken for each trial for qualitative analysis without regard to the scale of results, for the purpose of comparing results distributions of those collected studies presented in Chapter 2.

Table 3.2. Element details of cortical bone at the implant interface during the convergence test.

N_τ	N_S	L_τ (μm)	L_S (μm)	$\bar{L}$ (μm)
2	24	500	521	519
3	34	333	337	337
4	46	250	249	249
5	58	200	197	198
8	92	125	125	125
10	114	100	100	100

3.2.1 Mesh Details

The mesh described in Chapter 2 was modified to perform the convergence test. Modifications were applied to the number of divisions of the cortical shell thickness and interface perimeter, and the radially inflated element length. A set of experimental divisions was designated in the cortical shell according to a minimum of two divisions, and a maximum such that the mean edge length of the interface surface of each contact element was nearest to 100 μm. The number of perimeter divisions was calculated such that each element perimeter length was approximately equal to its shell thickness length. The mean interface length $\bar{L}$ was calculated for N_τ and N_S shell thickness and perimeter divisions, of shell thickness and perimeter element lengths L_τ and L_S, respectively (Table 3.2)

$$\bar{L} = \frac{N_\tau L_\tau + N_S L_S}{N_\tau + N_S}$$

Figure 3.1 shows the meshes that were used in the convergence test, according to Table 3.2. To capture a greater amount of information at the implant interface with cortical bone (compared to the mesh used in Chapter 2), the inflation algorithm was programmed such that the diameter of the layer of inflated elements was slightly less than the width of the planar surface of the crestal ridge. Some elements of notably low quality were present in some trials at the outer diameter of the inflated element layer, near the edge of the planar surface of the crestal ridge. The effects of these elements were assumed to be negligible because of the low magnitude of results in this region in the results from Chapter 2, and because of the significant distance from the implant interface of interest.

3.2.2 Material Properties

The isotropic, linear elastic material properties used in the convergence test were taken from those reported in [22] (Table 2.3): for cortical bone, Young's modulus of 13.7 GPa and Poisson's ratio 0.3, and for trabecular bone, Young's modulus 1.37

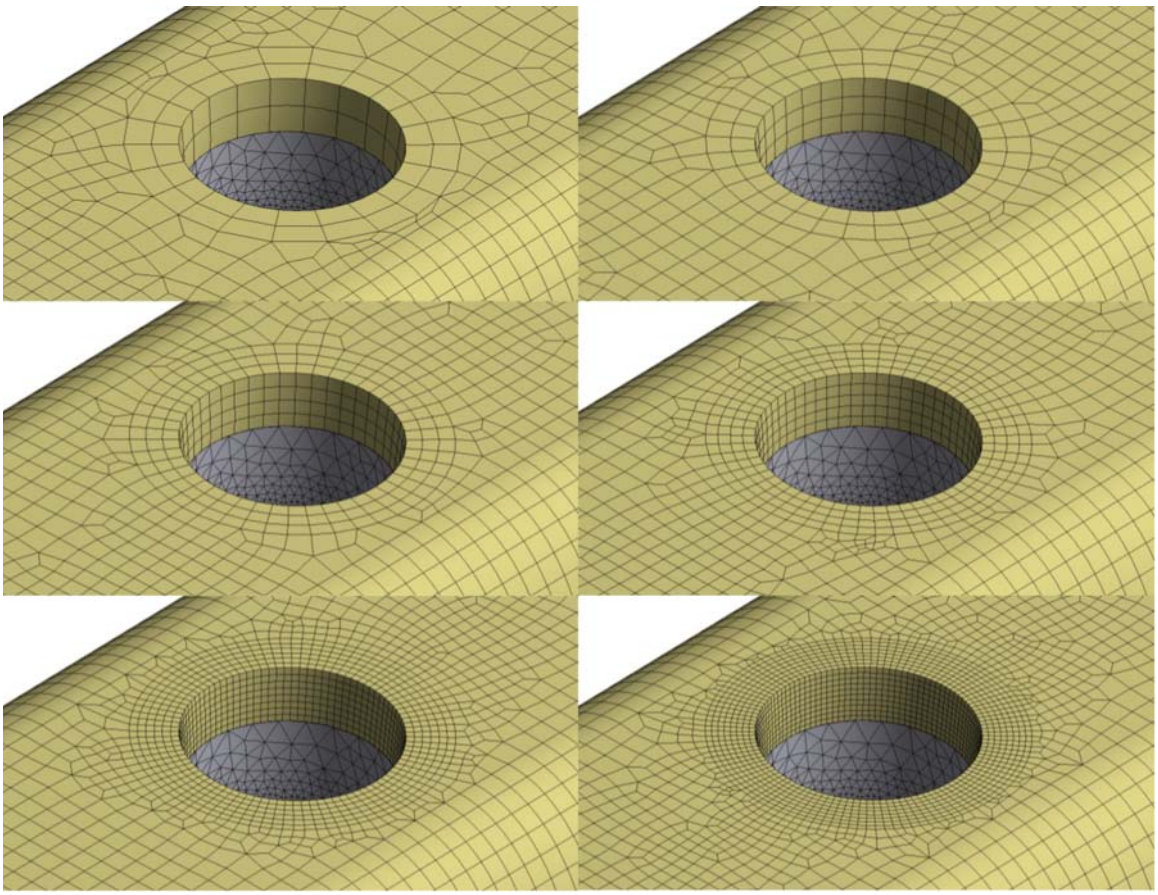

Figure 3.1. Meshes used in the convergence test, from 2 shell divisions (top left) to 10 (bottom right).

GPa and Poisson's ratio of 0.3. An equivalent yield strain ε_Y of 3,000 μ was used to implement the initiation of post-yield behavior during trials that considered plastic hardening [9]. A corresponding yield strength S_Y was calculated for cortical and trabecular bone according to the Generalized Hooke's Law and the material elastic Young's modulus E_{el}, where with a von-Mises stress yield criterion

$$S_Y = E_{el}\varepsilon_Y$$

For post-yield behavior, a plastic modulus E_{pl} was assigned to cortical and trabecular bone according to 5% bilinear hardening (that is, $E_{pl} = 0.05E_{el}$). Considering

Table 3.3. Elastic and post-yield material properties used during the convergence test.

	Elastic Properties		Post-Yield Properties	
	Young's Modulus (GPa)	*Poisson's ratio*	*Yield Strength* (MPa)	*Tangent Modulus* (MPa)
Cortical	13.7	0.30	41.1	685
Trabecular	1.37	0.30	4.11	68.5
Ti6Al4V	110	0.35	880	0

the von-Mises stress σ_{VM}, the elastoplastic tangent modulus $E = E(\sigma_{VM})$ of skeletal tissue during trials that considered plastic deformation was then

$$E = \begin{cases} E_{el} & \sigma_{VM} < S_Y \\ E_{pl} = 0.05 E_{el} & \sigma_{VM} \geq S_Y \end{cases}$$

The titanium alloy Ti6Al4V was assigned to the implant and loading post: Young's modulus of 110 GPa and Poisson's ratio of 0.35. Yielding was assumed to not occur in either part, and perfect plasticity was assigned to the implant and loading post (that is, $E_{pl} = 0$). The absence of yielding in both the implant and loading post was verified for each trial that considered plastic deformation (Table 3.3). For brevity, trials that did not consider plastic deformation are henceforth referred to as the elastic trials, and trials that considered plastic deformation are henceforth referred to as the plastic trials.

3.3 Results

Figure 3.2 shows the recorded maximum von-Mises stress and equivalent total strain in cortical bone for the elastic and plastic trials of the convergence test. For the elastic trials, at ten divisions of the cortical shell both the von-Mises stress and equivalent strain continued to diverge, and at an exponential rate with respect to

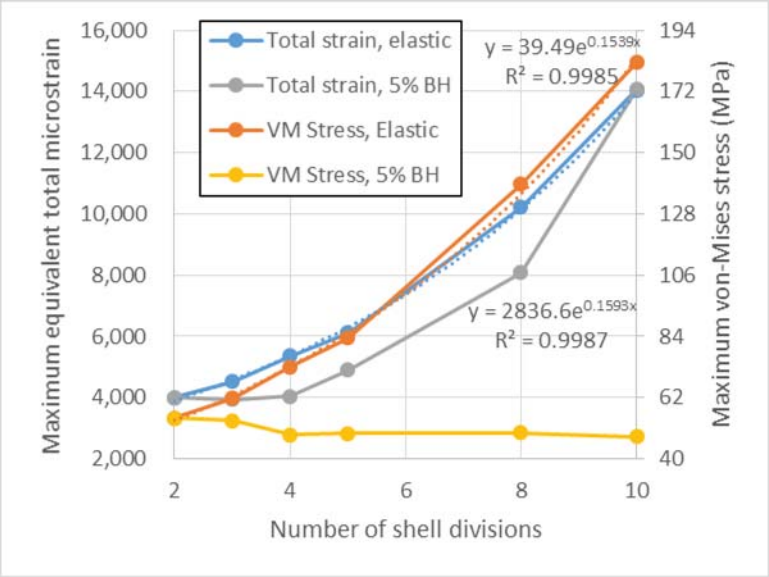

Figure 3.2. Maximum equivalent total strain and von-Mises stress in cortical bone vs. number of cortical shell divisions during the convergence test for elastic and 5% bilinear hardening (5% BH) material properties.

shell divisions. Maximum von-Mises stress and maximum equivalent total strain both fit an exponential curve with an R^2 value of 0.9985 and 0.9987, respectively. This implies that, for both stress and strain in cortical bone, at least one principal result is divergent in at least the range of tested mesh resolutions for a typical implant FE model setup. For the plastic trials, the maximum equivalent total strain was convergent for three shell divisions, and then diverged similarly to the elastic trials. The maximum von-Mises stress was convergent during all plastic trials.

Figure 3.3 shows the equivalent total strain distributions in the cortical shell for the elastic trials. For all elastic trials, a strain concentration was observed in cortical bone at the superior face of the crestal ridge, along the perimeter of the implant interface. Maximum stress and strain results were both found at this feature for all elastic material trials. For two and three shell divisions (Figure 3.3, top left and top right, respectively), results demonstrated strain distributions that were consistent with those reported in [14,39]. However, beginning at a thickness division of 4 (Figure

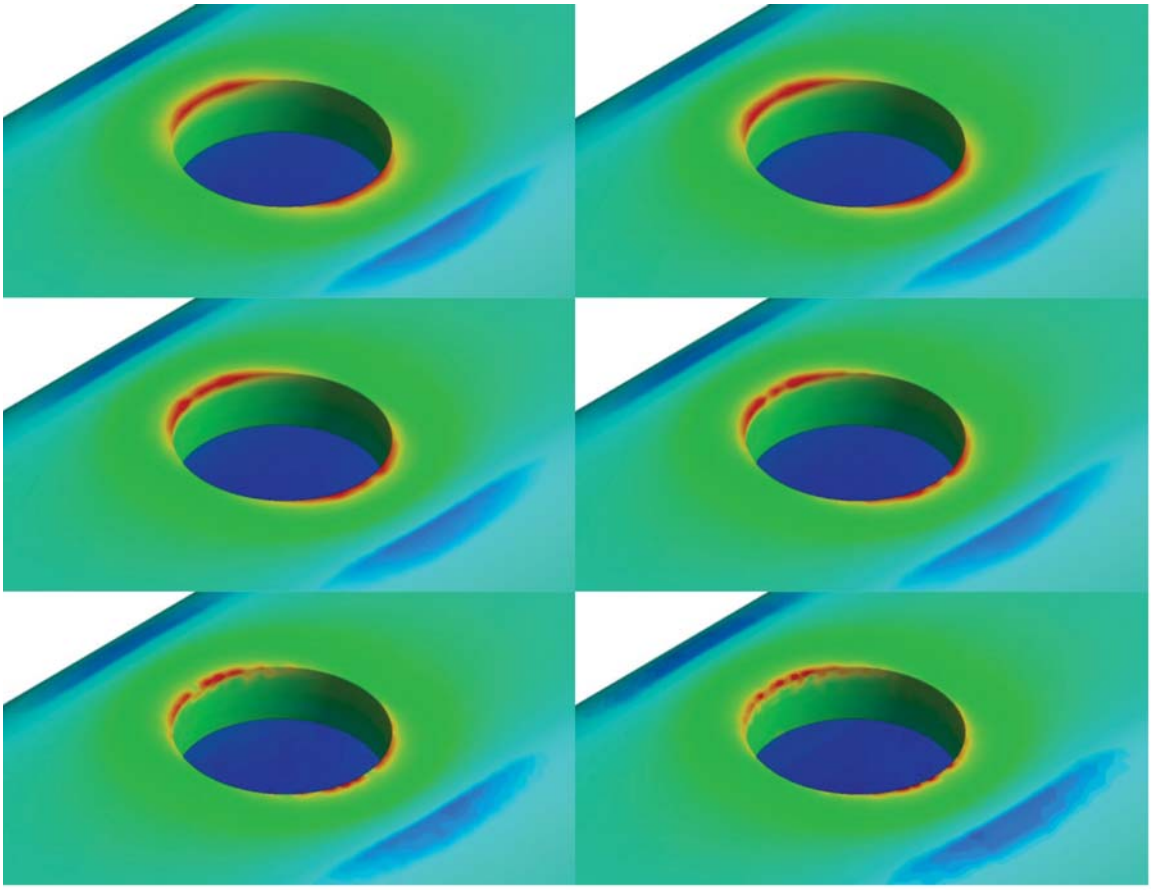

Figure 3.3. Equivalent total strain results of the convergence test neglecting plastic deformation, from 2 shell divisions (top left) to 10 (bottom right).

3.3, middle left), strain results were observed to begin to coalesce at the superior perimeter of the implant interface. This trend continued such that, for 8 and 10 shell divisions (Figure 3.3, bottom left and bottom right, respectively), distinct points of concentrated strain were evident.

Figure 3.4 shows the equivalent total strain distributions in the cortical shell for the plastic trials. Similarly to the elastic trials, a strain concentration was observed in cortical bone at the perimeter of the implant interface. Though the von-Mises stress results converged in the plastic trials, strain results continued to diverge with

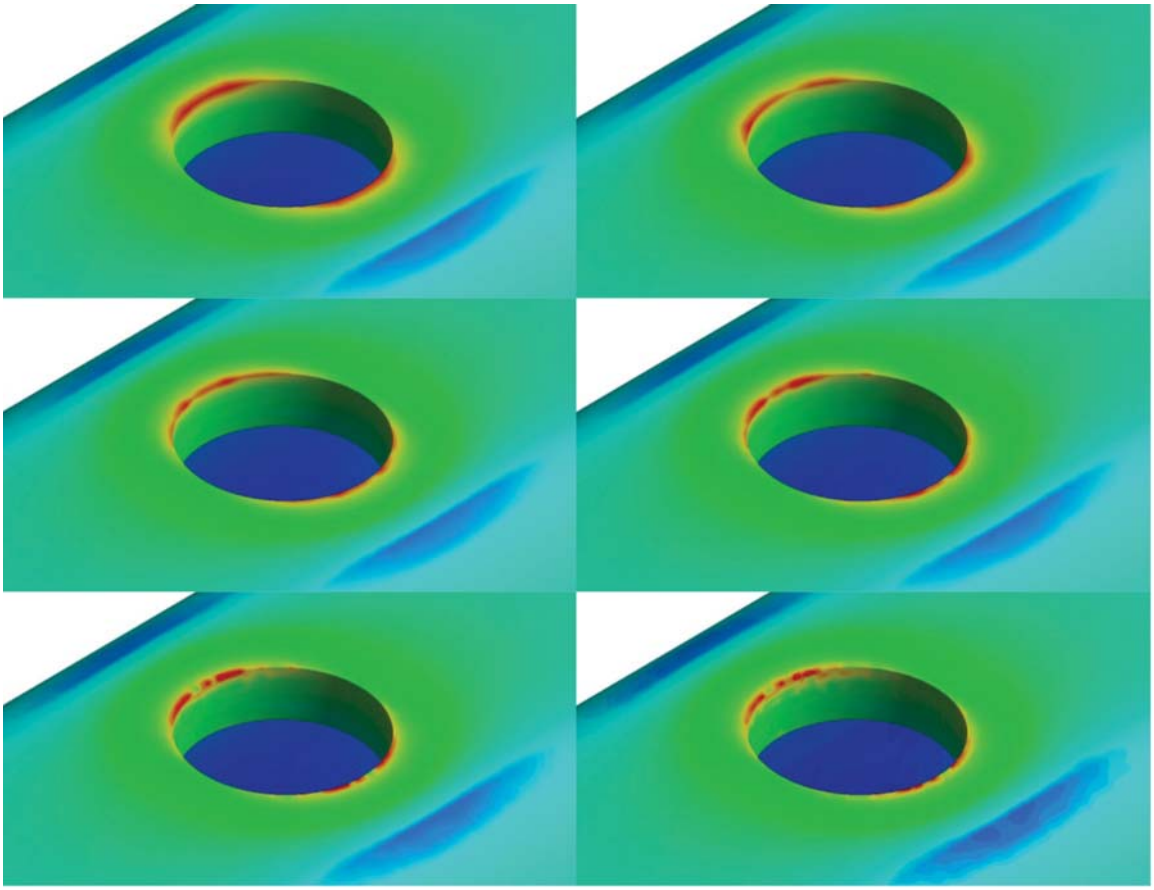

Figure 3.4. Equivalent total strain results of the convergence test considering 5% bilinear plastic hardening, from 2 shell divisions (top left) to 10 (bottom right).

increasing mesh resolution at the implant interface. For 8 and 10 shell divisions (Figure 3.4, bottom left and bottom right, respectively), distinct points of concentrated strain were evident.

3.4 Discussion

Results demonstrated the presence of significant stress and strain concentrations in cortical bone at the superior perimeter of the implant interface. As mesh resolution increased at this feature, maximum results continued to diverge, and results

distributions coalesced at distinct points of concentration. The coalescence of results distributions is observable in reported results from collected literature with which the proposed model strongly disagreed in Chapter 2 [22, 23], while reported results from collected literature of relative agreement demonstrated a more continuous response [14, 39]. Since no imperfections were modeled on the surface of the implant or cortical bone, no other potential explanation for these different results distributions was conceived except for the presence of a singular configuration [55]. Even though stress results converged in the plastic trials, the divergence of strain results demonstrated the persistence of this singular configuration in the model during plastic deformation with material hardening.

If indeed the typical implant FE model contains a singularity at the implant interface, then the positive correlation between mesh resolution and divergence of results is logically rational. While a stress singularity may have no physical meaning, theoretically it exists as an infinite value at a single point. In FEM, enclosing some point in a discrete volume and formulating a solution for the volume produces an approximate result near the point. By taking the limit of an enclosing volume about a singular point to zero, one would then calculate an infinite result, and this is one possible explanation for what occurred during the convergence test. This explanation is consistent with reported information in collected literature concerning implemented meshes: reported results distributions with the qualities of a singularity were produced from a model that implemented a high-resolution mesh at the suspected singular configuration [22,23], while reported results distributions from models with a more moderately sized mesh were without the qualities of a singularity [14, 39].

The existence of a singularity in the typical implant FE model diminishes some reliability of the typical implant FE model to assess implant design and predict implant stability. The mesh dependency of maximum results in cortical bone at the implant interface exposes a consequential dubiety about maximum results. Given the highly eccentric features of the implant interface with trabecular bone, it is reasonable to speculate that a singular configuration is also inherent in trabecular bone

under typical model assumptions. The singular configuration of the type by which the cortical-implant interface can be described requires the implementation of advanced formulations like cohesive and adhesive laws [55]. The undertaking of accumulating sufficient *in vivo* experimental data to develop such descriptions in non-negligible, neither is the added computational cost of implementing them in numerical methods like FEA.

An alternative solution is to utilize some other method of analysis and only consider maximum results in skeletal tissue in regards to fracture. While it is (presumably) insufficient to merely inspect FEA results of a simulation and disregard seemingly singular results, Figure 3.2 demonstrates that maximum results from spared results distributions can be unrepresentative of any meaningful prediction about the response in cortical bone. One alternative method of analysis has been proposed and utilized that calculated and statistically analyzed the volume of overloaded skeletal tissue in results [18]. Since results near the singular configuration in cortical bone were limited to the neighborhood of the strain concentration (Figures 3.3 and 3.4), this method of analysis may be more reliable when implemented with a well designed mesh. A similar method for analyzing results and predicting long-term stability is proposed and utilized in Chapter 4.

A second potential solution is the modeling of material softening (that is, damage) in bone. In the plastic trials, as stress in skeletal tissue entered the plastic region, the tangent modulus was reduced from the elastic range but remained positive. If the tangent modulus were negatively correlated with plastic strain instead, then the effects of the singularity may at least be isolated to a few nearby elements. Clinical observations support the implementation of material softening in skeletal tissue [49, 56]. Furthermore, the region of coalescing strain results from the convergence test has been clinically observed to be a site of significant bone loss [27]. Clinical data in literature supports the associations of high stresses, strains and damage accumulation with bone loss [57–59]. Chapter 5 presents a novel material model to describe the accumulation of damage in skeletal tissue and its effects on biomechanical events.

4. A DESIGN OF EXPERIMENTS TO STUDY THE EFFECTS AND SIGNIFICANCE OF THE CROWN-TO-IMPLANT RATIO ON LONG-TERM IMPLANT STABILITY

4.1 Introduction

The utilization of short implants is of notable interest to clinicians. When considering regions of limited bone height, short implants rectify the necessity for sinus lifting procedures, and therefore avoid additional cost and surgery. A major difficulty when selecting short implants is the biomechanical effects of increasing stress and strain distributions in skeletal tissue. When designing an implant superstructure for a region of limited bone height, a short implant length can be selected for a given crown height. An increasing crown height and decreasing implant length introduce a major design problem by increasing the resulting bending moment from lateral load components, and by decreasing the interface with skeletal tissue through which the bending moment is absorbed. In implant design, this phenomenon is represented by the C/I ratio. As the implant length decreases, an implant with an unfavorably high C/I ratio may induce higher concentrations of stress and strain in bone, which may cause occlusal overloading [60]. Occlusal overloading may cause significant biomechanical implant complications, including bone loss, loss of osseointegration and the loosening and/or fracture of prosthetics [61–63].

Considering mechanical quantities like stress and strain, the Mechanostat hypothesis proposes the relationship between skeletal structural adaptation and mechanical loading [64] as a potential redefining of Wolff's Law [65]. The Mechanostat suggests that repeated strain of a particular magnitude can be related to a functional response in skeletal tissue. Considering the effects of the C/I ratio, the hypothesis predicts that sufficiently high strain provokes bone loss and/or fatigue fracture, while more

moderate strain results in bone modeling or functional inactivity [57]. The relationship between the C/I ratio and the presence of biomechanical implant complications has been widely investigated in literature and, though previous clinical studies failed to approve the influence of the C/I ratio on bone loss [27, 66], the use of FEA models [20, 23] and photoelastic analyses (PEA) [24, 29] have shown a positive correlation between C/I ratio and stress and/or strain distribution.

Among experimental sets with various C/I ratios, reported results for a varying C/I ratio demonstrated similar stress and strain distributions under pure axial loading, whereas lateral load components caused significantly concentrated results in surrounding bone regions opposite to force application. Moreover, all results from reviewed literature agreed that oblique loading could cause greater biomechanical effects on the implant-bone system [20, 23, 24, 29]. However, the suggestion has been made based that the crown height may have a more significant role than the C/I ratio on the resulting stress distribution [24].

In regards to clinical applications, several limitations have been found in previous FEA and PEA studies: (1) C/I ratios greater than 2.0 were scarcely evaluated; (2) orthotropic material properties and nonlinear effects were both typically neglected; (3) most of the available models either did not consider the thread features in the implant-bone system interface or lacked a sufficient level of detail to accurately predict localized effects of stress and/or strain; and (4) maximum stress and/or strain results were typically exclusively evaluated, with little to no consideration of the functional response of the entire site.

The present study sought to evaluate the functional effects and significance of the C/I ratio in a single implant-supported crown by laterally loading a set of implants with various crown heights and implant lengths. The hypothesis of the study is that the increase of the C/I ratio can be associated with greater likelihood of widespread overloading in bone by augmenting the strain concentrations associated with an implant design, and therefore diminishes the likelihood of long-term implant stability.

4.2 Materials and Methods

To study the effects of the C/I ratio on the long-term stability of a dental implant, the parameterized FE model described in Chapter 2 was exported and adapted. A DOE was constructed that considered two four-level parameters (implant length and C/I ratio) for a total of 16 experiments. Nonlinear FEA under static loading was applied to implant lengths (IL) of 6.0, 8.0, 10.0 and 12.0 mm and C/I ratios 1.0, 1.5, 2.0 and 2.5. A uniform thickness of 1 mm was assigned to cortical bone. The assumptions of continuous tissue, perfect osseointegration and perfect implant integration were utilizied. The mesh was designed per Chapter 2, and the cortical shell was divided into three element thickness layers per results of the convergence test in Chapter 3. FEA was performed in ANSYS v15.0 on a personal computer, Intel i7-4790k (4.00 GHz) processor, 16.0 GB RAM. For brevity, implant configurations are denoted [implant length in mm / crown-to-implant ratio] (for example, a configuration of an implant length of 6.0 mm and C/I ratio of 2.5 is denoted [6.0/2.5]).

4.2.1 A Novel Method to Analyze Long-Term Stability

For each experiment, the FE model mesh connectivity and equivalent microstrain nodal results of each tissue at the implant interface were imported in Matlab R15a (MathWorks, Massachusetts, USA). By cross-referencing the model connectivity and nodal results, all elements of each tissue in contact with the implant were isolated. For each contact element, the contact surface area and its mean result were calculated, where the mean result was calculated from the nodes that define the contact surface area and, for the two vectors p_i and q_i and permutation operator ϵ_{ijk}, the surface area A was calculated as

$$A = \frac{1}{2}\sqrt{\epsilon_{ijk}\epsilon_{imn}p_j p_m q_k q_n}$$

For tetrahedral elements, p_i and q_i originate from one vertex and define two adjacent sides of the contact surface triangle, and for hexahedral elements the vectors define the two diagonals of the contact surface planar convex quadrilateral. The total implant

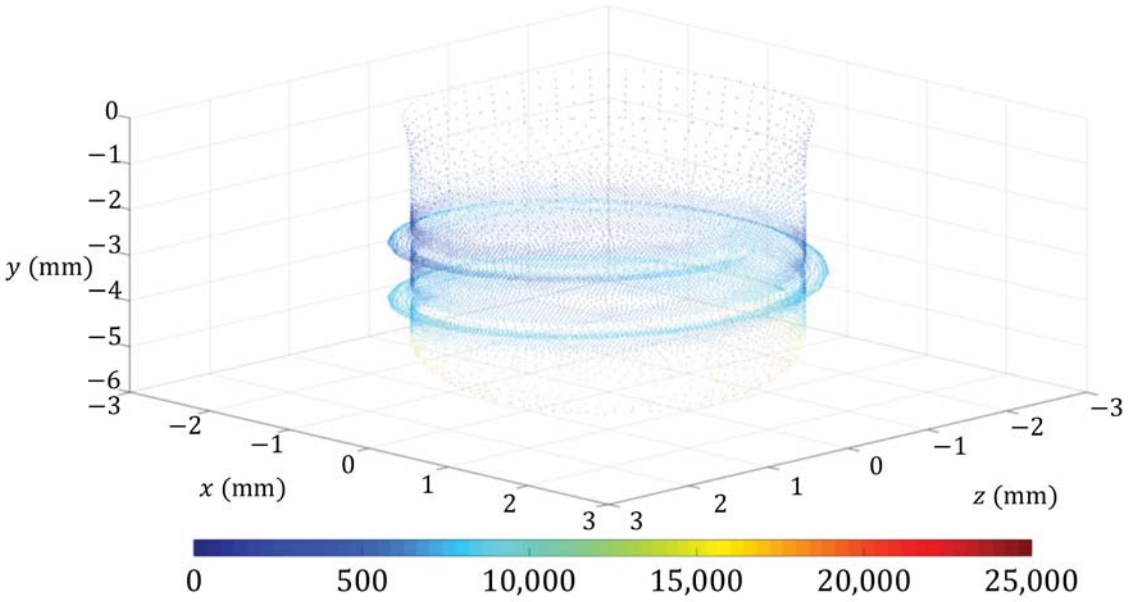

Figure 4.1. Sample of imported equivalent strain nodal results at the implant interface in Matlab R15 for IL = 6 mm, C/I = 2.5.

interface surface area was calculated by summing all of the contact element surface areas of the implant interface in both bones. The contact surface area for each elements was allocated by functional response to their mean surface results according to Table 4.2. The percent surface area of each functional response was then calculated by dividing the total surface area of the response by the total surface area of the implant interface (Figure 4.1). Predictions about long-term stability of the implant were made by comparing and extrapolating from the calculated functional responses of the configurations [12.0/1.0] and [6.0/2.5], where the former and latter were assumed to be the most and least stable, respectively.

4.2.2 Material Properties

Previous studies have been completed to describe local anisotropy in bone tissue [38, 67], which in FEA demonstrates significant effects in predicted stress and strain

Table 4.1. Orthotropic elastic material properties in the C/I Effects DOE.

	Young's Moduli (GPa)			Poisson's ratio			Shear Moduli (GPa)		
Direction	x	y	z	xy	yz	xz	xy	yz	xz
Cortical	10.5	14.2	22.9	0.23	0.12	0.13	3.7	6.0	4.8
Trabecular	0.32	0.39	0.96	0.25	0.12	0.10	0.13	0.17	0.09
Ti6Al4V	110	110	110	0.35	0.35	0.35	41	41	41

results [38–40]. In the proposed model, linear elastic, orthotropic properties were assigned to cortical and trabecular bone while studying the effects of the C/I ratio. Elastic material properties for cortical and trabecular bone were obtained [40] and rotated into the orientation of the proposed model. The isotropic properties of the titanium alloy Ti6Al4V were assigned to the implant and loading post (Table 4.1).

4.3 Results

Though there is no general consensus on results of interest in skeletal tissue (Chapter 2), the Mechanostat hypothesis [64] has been successful at predicting the functional response of skeletal tissue to mechanical strain [9]. The effects of the C/I ratio on bone tissue health were evaluated accordingly. Through the microstrain results distribution in cortical and trabecular bone, the corresponding biological response in skeletal tissue was predicted according to reported functional responses to various microstrain values [68] (Table 4.2).

4.3.1 Results of the Strain Distribution Response

For all C/I ratios of the DOE, the maximum equivalent strain in cortical bone was observed at the perimeter of the implant interface, on the superior surface of the crestal ridge (Figure 4.2). In trabecular bone, the maximum equivalent strain

Table 4.2. Biomechanical funtional response categories.

Function range	Range values (μ)	Functional response
Disuse	$0 - 100$	Bone resorption
Remodeling	$100 - 300$	Bone repair
Modeling	$2,000 - 4,000$	Bone growth
Overloading	$4,000 - 25,000$	Irreversible creep
Fracture	$> 25,000$	Failure

was found at the inferior termination of the thread feature. For the configuration [12.0/1.0], overloading strain in cortical bone occurred at the superior face of the crestal level, at the strain concentration discussed in Chapter 3 and where crestal bone loss has been observed *in vivo* [32,69,70]. In trabecular bone, overloading strain occurred at the radially extreme thread features of the implant interface and the superior interface with cortical bone. A significant region of overloading also occurred in trabecular bone at the inferior interface with the implant. With increasing C/I ratio, modeling and overloading in both tissues became more prominent at these features, and more widespread throughout the crestal ridge.

As implant length decreased, the individual effects of each overloading feature in trabecular bone became less apparent, and their prevalence continued to increase with increasing C/I ratio. For an implant length of 6.0 mm, widespread overloading in trabecular bone occurred for C/I ratios greater than 1.5, as well as for the configuration [8.0/2.5]. For the configurations [8.0/2.0], [10.0/2.0], [10.0/2.5] and [12/2.5], some overloading occurred at the cylindrical feature of the implant interface. For all implant lengths, significant overloading occurred at the inferior implant interface, and at least to some degree at the thread features of the interface. Fracture was recorded in trabecular bone for the configurations [6.0/2.0], [6.0/2.5], [8.0/2.5] and [10.0/2.5]. No apparent correlation between implant length and maximum equivalent strain was demonstrated, presumably because of the changing orientation of the inferior thread

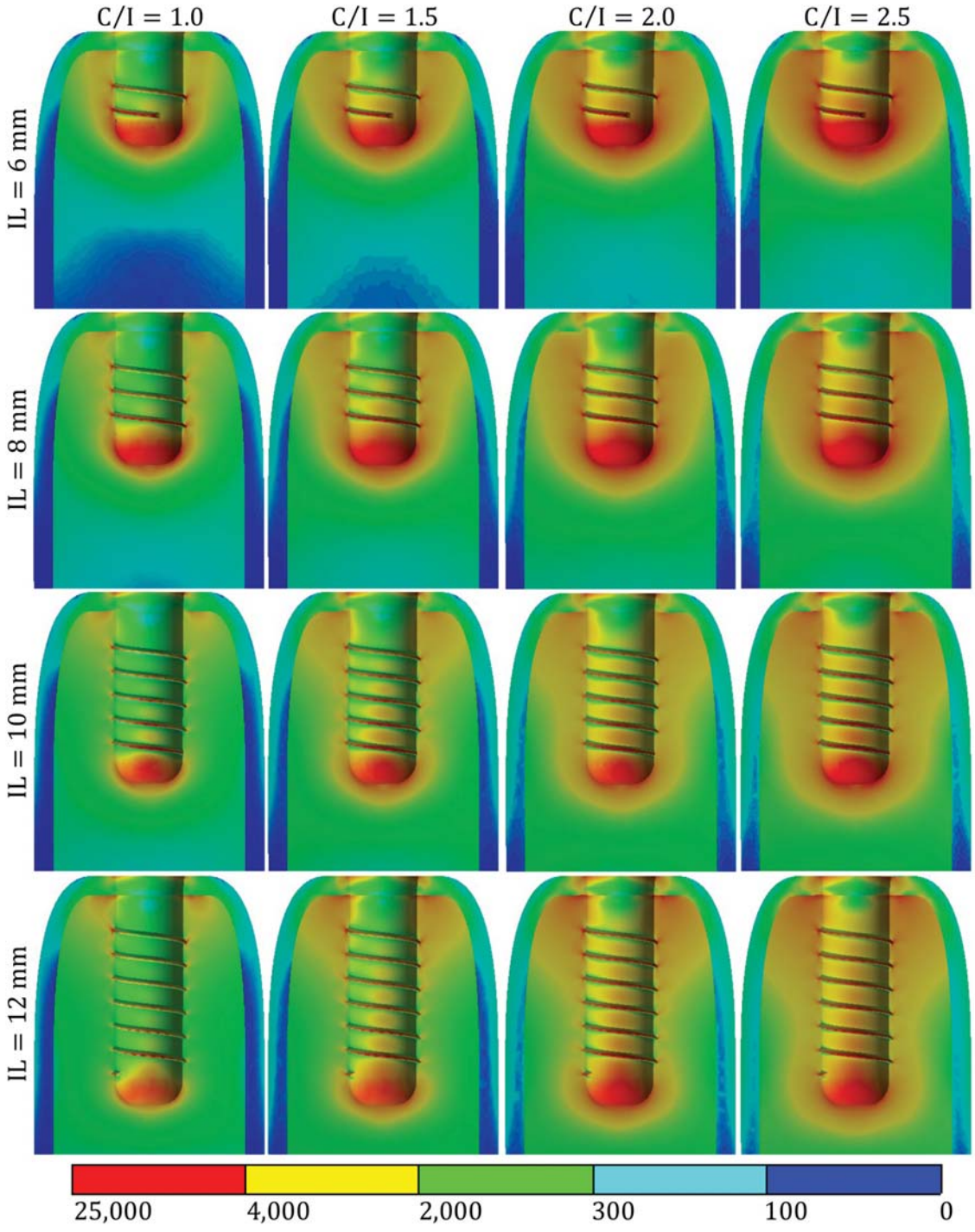

Figure 4.2. Cross-sectional equivalent strain results sample in skeletal tissue for all configurations of the C/I Effects DOE. Results are scaled according to Table 4.2.

termination with respect to the plane of loading (Figure 4.3). Interestingly, in cortical bone the maximum equivalent strain was greater for larger implant lengths, and was nearly equal for implant lengths of 6.0 and 8.0 mm. If an overloading maximum equivalent strain can be associated with bone loss, then results from Figure 4.3 would predict that short implant lengths cause less bone loss in cortical bone. However, the prediction of significantly more overloading and consequential bone loss in cortical bone for implant lengths of 10.0 and 12.0 mm compared to those of 6.0 and 8.0 mm is inconsistent with results in Figure 4.2.

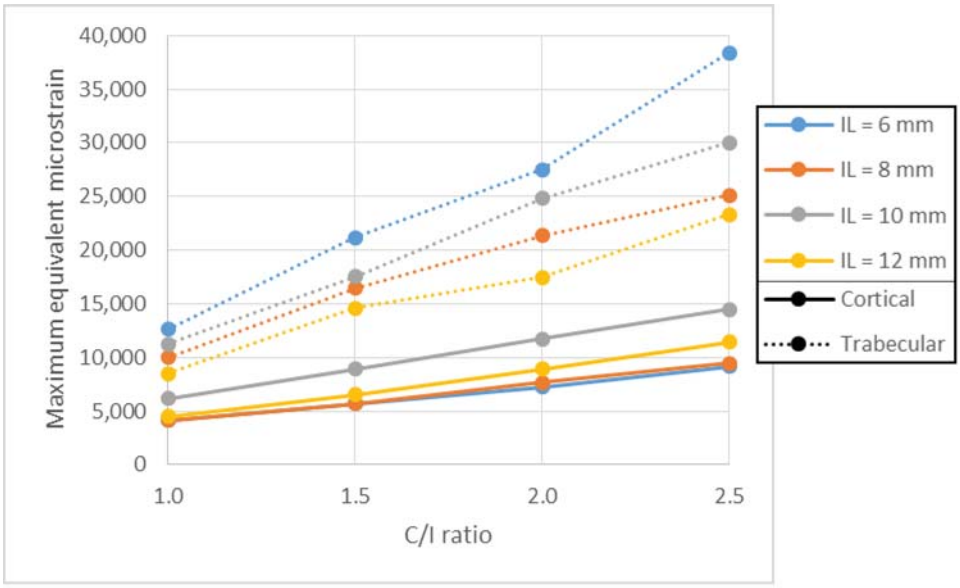

Figure 4.3. Maximum equivalent strain results in cortical and trabecular bone vs. C/I ratio for all configurations of the C/I Effects DOE.

4.3.2 Results of the Implant Interface Considering Long-Term Stability

As demonstrated and discussed in Chapter 3, the maximum equivalent strain may not be sufficiently representative of results from FEA. Since a high-fidelity mesh may exaggerate the inherent strain concentrations of the eccentric features of the implant interface, further evaluation of strain in skeletal tissue at the implant interface was

performed by statistical analysis. The general consistency of the predicted functional response in skeletal tissue at the implant interface was evaluated under the conditions of preceding biomechanical inactivity without pending bone remodeling, for the purpose of assessing the likelihood of long-term implant stability.

Figure 4.4 shows the results of two predicted functional responses from statistical analysis of the implant interface in both tissues. The functional responses of modeling, inactivity (that is, a lack of functional response) and overloading were chosen for comparative evaluation, to observe the likelihood of continued implant integration. The functional responses of disuse, remodeling and fracture were all observed to be negligible for this analysis (less than 0.22% contribution, at most). Results demonstrated a negative correlation between the C/I ratio and the functional response of inactivity, and a positive correlation with overloading in tissue. The extrema of percent inactivity both occurred for an implant length of 12.0 mm, where the most percent inactivity occurred for the configuration [12.0/1.0], and the least occurred for [12.0/2.5]. For all C/I ratios, the most and least percent overloading occurred for an implant length of 6.0 and 12.0 mm, respectively. The sensitivity of percent inactivity to changing crown height was greatest for a C/I ratio of 1.0 and steadily decreased, while the sensitivity of percent overloading to crown height was generally constant.

For C/I ratios greater than 1.0, a positive correlation was observed between percent modeling and implant length. For implant lengths of 10.0 and 12.0 mm, results predicted a seeming parabola with a maximum somewhere near a C/I ratio of 1.75, while for implant lengths of 6.0 and 8.0 mm, percent modeling peaked at a C/I ratio of 1.5 and then steadily decreased. Modeling for an implant length of 6.0 mm marginally increased from a C/I ratio of 1.0, and marginally decreased from the configuration [10/1.5]. Modeling for an implant length of 12.0 mm was predicted to slightly increase from a C/I ratio of 1.5, which may explain the unique trend of predicted inactivity for the 12.0 mm implant length from Figure 4.4: the interface of a 12.0 mm implant length transitions more quickly from inactivity into modeling than from modeling into overloading.

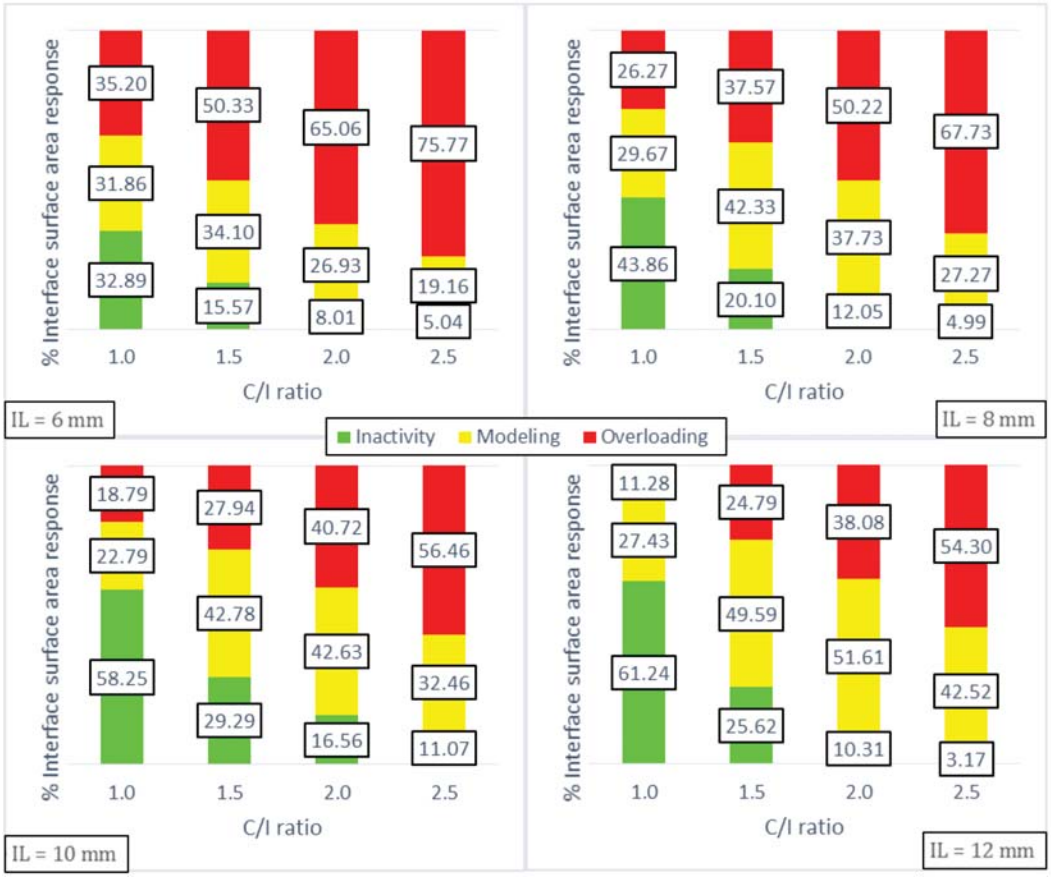

Figure 4.4. Percent surface area of the implant interface in tissue with the predicted functional responses modeling (green), inactivity (yellow) and overloading (red), according to Table 4.2.

4.4 Discussion

From the results in Figure 4.2, the configuration [12.0/1.0] demonstrated the sources of significant strain concentrations at the implant interface. Even for this configuration, maximum equivalent microstrain results in Figure 4.3 were within the range of overloading for cortical and trabecular bone (4,500 μ and 8,475 μ, respectively), and so for even the most conservative configuration of the study some degree of overloading occurred. As results showed, when the C/I ratio increases, overloading becomes more prevalent, while at lower C/I ratios and larger implant lengths the individual strain concentrations were distinctly observable. Concerning the biome-

chanical complications of overloading strain in skeletal tissue, the C/I ratio then augments the the inherent risks of a particular implant design, especially concerning interfacial features (for example, thread profile, thread pitch, etc.). Neglecting relevant innovations in materials, surface finish and patient-specific design, higher C/I ratios may then be achievable for implants with interfacial features that are less likely to induce overloading strain concentrations in skeletal tissue.

Concerning results in Figure 4.4, the configuration [12.0/1.0] can be characterized by a high percent of predicted inactivity and low percent overloading at the implant interface. Contrasted with the configuration [6.0/2.5], where the interface was predicted to consist mostly of overloading and marginally of inactivity, a set of criteria was selected to predict the likelihood of long-term implant stability. Since the former and latter configurations are reasonably presumed to be the most and least advisable concerning implant stability, respectively, a configuration that induces excessive amounts of overloading compared to inactivity is considered volatile at best, to clinically inadvisable at worst. A configuration that induces marginal overloading and mostly inactivity is considered clinically advisable. In cases between these extrema, the predicted response of modeling, results distributions and biological factors may provide further insight into predicting long-term stability of a configuration.

By this paradigm, an implant length of 6.0 mm is considered to be the most inadvisable of those considered. For [6.0/1.0] a nearly equal third of the interface surface area was predicted to undergo the three functional responses of interest, which is considered as highly volatile. As the C/I ratio increases, the assessment further deteriorates as percent modeling is predicted to subside while overloading increases and inactivity decreases. More than half of the interface was predicted to experience overloading for this implant length and all C/I ratios greater than 1.0, with a minority of the response consisting of inactivity and modeling. Therefore, C/I ratios greater than 1.0 for an implant length of 6.0 mm are predicted to be clinically inadvisable.

For the configuration [8.0/1.0], results at the interface predicted a significantly larger consistency of inactivity than overloading (difference of 18%), and marginally

more modeling than overloading (difference of 3%). For [8.0/1.5], overloading was predicted to be greater than inactivity (difference of 17%), though this is perhaps mitigated by the majority consistency of predicted modeling (42%). This may imply that the configuration [8.0/1.5], though not conclusively inadvisable, is expected to be undergo significant amounts of structural adaptation. *In vivo*, no biological factors that may inhibit modeling and remodeling processes could then be present to confidently predict long-term stability. Consequentially, all C/I ratios greater than 1.5 for an implant length of 8.0 mm are predicted to be clinically inadvisable.

For [10.0/1.5] and [12.0/1.5], marginally greater amounts of inactivity were predicted than overloading (differences of 1.4% and 0.8%, respectively), and the majority of predicted response was modeling (43% and 50%, respectively). Considering the distributions in Figure 4.2, where the majority of overloading for these two configurations occurred in trabecular bone at the inferior surface of the implant interface, these two configurations under ideal biological conditions may become more stable. For [10.0/2.0] and [12.0/2.0], inactivity became the minority predicted response, and results imply the necessity of suitable biological conditions for significant structural adaptation. This was especially the case for an implant length of 10.0 mm, where modeling was only marginally greater than overloading (difference of 2%), while for an implant length of 12.0 mm modeling remained significantly greater (difference of 14%). This implies that the configuration [10.0/2.0] may be considered as highly volatile, while [12.0/2.0] may be considered moderately so. A C/I ratio of 2.5 for both implants lengths is predicted to be clinically inadvisable.

The validity and limitations of this method of assessment are currently unknown and should be subject of future research. The present application of the method is likely a highly simplified version of what could be its final process, where more advanced (and even patient-specific) FE models could be implemented to assess more implant configurations and multiple load cases. Refinement of the method should also be cross-referenced with literature and reconciled with clinical data on long-term success rates. Within the scope of the present study, the assessment of all

configurations of the DOE are summarized in Table 4.3, where percent overloading $\%O$ is shown, with the calculated differences in the responses of inactivity ($\Delta\%I$) and modeling ($\Delta\%M$) compared to overloading.

Table 4.3. Summary of assessments of all C/I Effects DOE implant configurations.

Implant length (mm)	C/I ratio	$\%O$	$\Delta\%I$	$\Delta\%M$	Assessment
6.0	1.0	35	-2	-3	Volatile
6.0	1.5	50	-35	-16	Inadvisable
6.0	2.0	65	-57	-38	Inadvisable
6.0	2.5	76	-71	-57	Inadvisable
8.0	1.0	26	18	3	Advisable
8.0	1.5	38	-17	5	Volatile
8.0	2.0	50	-38	-12	Inadvisable
8.0	2.5	68	-63	-40	Inadvisable
10.0	1.0	19	39	4	Advisable
10.0	1.5	28	1	15	Advisable
10.0	2.0	41	-24	2	Volatile
10.0	2.5	56	-45	-24	Inadvisable
12.0	1.0	11	50	16	Advisable
12.0	1.5	25	1	25	Advisable
12.0	2.0	38	-28	14	Volatile
12.0	2.5	54	-51	-12	Inadvisable

5. A MULTISCALE MATERIAL MODEL TO PREDICT THE BIOMECHANICAL RESPONSE OF BONE TO SHORT-TERM DAMAGE ACCUMULATION

5.1 Derivations

5.1.1 Background Theory

From the experimental correlation from [71], the Young's modulus E is a function of the apparent density ρ

$$E(\rho) = B\rho^{\beta} \tag{5.1}$$

where B and β are material parameters and ρ is related to the maximum density $\hat{\rho}$ by the porosity n

$$\rho = \hat{\rho}(1 - n) \tag{5.2}$$

[72] proposes a relationship between the tensorial damage d_{ij}, as proposed in [73], and a remodeling tensor h_{ij}

$$d_{ij} = \delta_{ij} - h_{ik}h_{kj} \tag{5.3}$$

where δ_{ij} is the second-order Kronecker-delta. h_{ij} is proposed in [72] to also be related to the density of the material while considering the directionality of porosity by a fabric tensor $\hat{h}_{ij}$

$$\begin{gathered} \left(\frac{\rho}{\hat{\rho}}\right)^{\beta/2} \hat{h}_{ij} = h_{ik}h_{kj} \\ \det(\hat{h}_{ij}) = 1 \end{gathered} \tag{5.4}$$

In the model from [72], h_{ij} are internal state variables that relate the damage in bone to the stimulation of a bone mass rate $\dot{\rho}$ by the Cauchy stress tensor σ_{ij} from loading, such that

$$\dot{\rho} = \dot{\rho}(h_{ij}, \sigma_{ij}) \tag{5.5}$$

Partial motivation of the model from [72] is to relate the future state of the material to its current material and loading states, so to predict the anisotropic evolution of the material in response to mechanical stimulus. As an example, according to [74] the evolution of the elasticity tensor C_{ijkl} is directly influenced by ρ and β from (5.1) and by the loading state of stress and strain ε_{ij} tensors (see Appendix for relationship between C_{ijkl} and h_{ij})

$$\dot{C}_{ijkl}(\rho, \dot{\rho}, \sigma_{ij}) = \frac{\beta\dot{\rho}}{\rho} \frac{\sigma_{ij}\sigma_{kl}}{\sigma_{pq}\varepsilon_{pq}} \tag{5.6}$$

where by the Generalized Hooke's Law

$$\sigma_{ij} = C_{ijkl}\varepsilon_{kl} \tag{5.7}$$

So by combining (5.5) amd (5.6)

$$\dot{C}_{ijkl} = \dot{C}_{ijkl}(h_{ij}, \sigma_{ij}) \tag{5.8}$$

The state variables of the proposed model are then defined as h_{ij}, such that the material state evolves as a function of its state variables and mechanical stimulus.

5.1.2 Motivation for a Novel Material Model

A limitation of the model proposed in [72] is that the evolution of the material state is only influenced by the physiological response to mechanical stimulus. This fails to account for experimental results where material softening occurred in cortical bone specimens under compressive loading at microstrain values as low as 1,200 μ in middle-aged adults [49]. This is particularly relevant since, according to the Mechanostat hypothesis [64], bone modeling occurs at microstrain values between 2,000 and 4,000 μ [68]. Given the widespread success of the Mechanostat, its unification with the model from [72] and the reported experimental results in [49] necessitates that the mathematical description of skeletal adaptation considers the short-term accumulation of damage in response of mechanical stimulus.

Furthermore, results from Chapter 3 indicated that the assumptions of the typical implant FE model likely produce a singular configuration [55] in cortical bone. In the

convergence test, strain results in cortical bone from loading were shown to be mesh-dependent under typical modeling conditions. These conditions may include linear, perfectly elastic material modeling of bone with the neglect of material softening, and the modeling of the implant interface as perfectly bonded. Since the post-yield softening of cortical bone was well quantified experimentally [49] and material softening may be able to mitigate the singular configuration (Section 3.4), the present work seeks to propose a post-yield model of bone that considers the accumulation of microdamage from loading in terms of the state variables defined in [72].

5.1.3 General Formulation

Let the scalar damage D be defined as

$$D = 1 - \sqrt{\frac{E}{\hat{E}}} \tag{5.9}$$

where $\hat{E}$ is the Young's modulus of the material in its undamaged state $\hat{\rho}$

$$\hat{E} = E(\hat{\rho}) \tag{5.10}$$

such that, by combining (5.1), (5.9) and (5.10), for a reduced effective virtual state of density ρ^{re}

$$D = 1 - \left(\frac{\rho^{re}}{\hat{\rho}}\right)^{\beta/2} \tag{5.11}$$

(5.3) and (5.4) may then be written sequentially as

$$d_{ij} = \delta_{ij} - (1 - D)\hat{h}_{ij} = \delta_{ij} - h_{ik}h_{kj} \tag{5.12}$$

From [49], E is related to the (presumably) equivalent total strain ε relative to a threshold strain ε^o in a material of strain sensitivity A^ε and initial Young's modulus E^o

$$E(\varepsilon) = E^o e^{-A^\varepsilon(\varepsilon - \varepsilon^o)}; 0 < \varepsilon^o \leq \varepsilon \tag{5.13}$$

If ρ^o is the initial density before loading, then according to the form of (5.11), let D^L be the accumulated damage during loading

$$D^L = 1 - \left(\frac{\rho^{re}}{\rho^o}\right)^{\beta/2} \tag{5.14}$$

Similarly, writing D^L in the form of (5.9) and (5.13),

$$D^L = \sqrt{\frac{E(\varepsilon)}{E^o}} = 1 - e^{-\frac{A^\varepsilon}{2}(\varepsilon - \varepsilon^o)} \tag{5.15}$$

and setting (5.14) equal to (5.15) produces an expression for ρ^{re} during loading

$$\rho^{re}(\varepsilon) = \rho^o e^{-\frac{A^\varepsilon}{\beta}(\varepsilon - \varepsilon^o)} \tag{5.16}$$

that can be substituted into (5.1) to produce an expression for E as a function of ε for the initial state before loading ρ^o

$$E(\varepsilon) = \rho^o e^{-\frac{A^\varepsilon}{\beta}(\varepsilon - \varepsilon^o)} \tag{5.17}$$

and into (5.9) to produce an expression for D as a function of ε for ρ^o

$$D = 1 - \left(\frac{\rho^o}{\hat{\rho}}\right)^{\beta/2} e^{-\frac{A^\varepsilon}{2}(\varepsilon - \varepsilon^o)} \tag{5.18}$$

5.1.4 Reconciliation with the Mechanostat by Variable Strain Sensitivity

To reconcile the proposed material model with the Mechanostat and the observation of that the yield strain ε^Y of cortical bone is relatively unchanged by damage [75], a non-constant strain sensitivity is implemented to parameterize (5.18) to a novel material parameter D^U, an ultimate scalar damage at which material failure occurs for an ultimate strain ε^U. Let

$$\varepsilon^o = \varepsilon^Y < \varepsilon^U; D^U = D(\varepsilon^U) \tag{5.19}$$

such that, from (5.18)

$$D^U = 1 - \left(\frac{\rho^o}{\hat{\rho}}\right)^{\beta/2} e^{-\frac{A^\varepsilon}{2}(\varepsilon^U - \varepsilon^Y)} \tag{5.20}$$

which establishes the domain

$$0 < D^U < 1 \tag{5.21}$$

Rewriting (5.20) in terms of A^ε

$$A^\varepsilon = -\frac{2}{\varepsilon^U - \varepsilon^Y} \ln\left[\left(\frac{\rho^o}{\hat{\rho}}\right)^{-\beta/2} (1 - D^U)\right] \tag{5.22}$$

and defining an initial scalar damage D^o from (5.11) as

$$D^o = 1 - \left(\frac{\rho^o}{\hat{\rho}}\right) \tag{5.23}$$

by substituting (5.22) and (5.23) into (5.18) an expression for the scalar damage is produced that describes its evolution from the commencement of damage through to mechanical failure

$$D(\varepsilon) = 1 - (1 - D^o)\left[\frac{1 - D^U}{1 - D^o}\right]^{\frac{\varepsilon - \varepsilon^Y}{\varepsilon^U - \varepsilon^Y}} \tag{5.24}$$

5.1.5 Post-Yield Behavior

For a rate-independent plasticity model with a scalar yield criterion σ^Y, the plastic flow potential $f(\sigma_{ij})$ is a scalar function through which σ^Y is also defined. From the Generalized Hooke's Law, let

$$\sigma^Y = E\varepsilon^Y \tag{5.25}$$

or, by rewriting (5.9)

$$\sigma^Y(D) = (1 - D)^2 \hat{E}\varepsilon^Y \tag{5.26}$$

Implementing an associative flow rule, σ_{ij} and the plastic strain tensor ε_{ij}^{pl} are related by a plastic multiplier λ and a change in f with respect to σ_{ij}

$$d\varepsilon_{ij}^{pl} = \lambda \frac{\partial f}{\partial \sigma_{ij}} \tag{5.27}$$

The softening law $F(\sigma_{ij}, D)$ then states that the yield criterion changes with the plastic flow potential

$$F(\sigma_{ij}, D) = f(\sigma_{ij}) - \sigma^Y(D) = 0 \tag{5.28}$$

Since bone is observed to handle shear stress [1], let σ^Y be equal to the von-Mises stress

$$\begin{aligned} f(\sigma_{ij}) &= \sqrt{\frac{3}{2} s_{ij} s_{ij}}; \\ s_{ij} &= \sigma_{ij} - \frac{1}{3}\sigma_{kk}\delta_{ij} \end{aligned} \tag{5.29}$$

Assuming that the directional effects associated with a single load case are negligible compared to those from long-term, cyclical loading

$$\dot{\hat{h}}_{ij} = 0_{ij} \tag{5.30}$$

such that, for a single load case, from (5.12)

$$\frac{d}{dt}(h_{ik}h_{kj}) = -\dot{D}\hat{h}_{ij} \tag{5.31}$$

5.1.6 Damage-Induced Remodeling at the Continuum Level

A skeletal control volume V and density before loading ρ^o experiences a plastic strain ε_{ij}^{pl} from loading, the microdamage of which affects a partitioning of V into two regions of volume, one of which during the remodeling process is unaffected (V^{UD}) and one that during the remodeling process experiences resorption and formation processes (V^D). Knowing that the volume is unchanged

$$V = V^{UD} + V^D + V^v \tag{5.32}$$

where V^v is the volume of voids and is related to V through the porosity n or, considering the volume of mass V^m

$$n = \frac{V^v}{V} = 1 - \frac{V^m}{V} \tag{5.33}$$

Let $\rho^{re} = \rho^{re}(t)$ during remodeling, such that at time t

$$\rho^{re}(t) = \hat{\rho}(1 - n^{re}(t)) = \hat{\rho}(1 - D(t))^{2/\beta} \tag{5.34}$$

where n^{re} is the reduced effective porosity of V after loading. From (5.16) and (5.24), immediately after loading (at time $t = 0$) and for an ultimate plastic strain $\varepsilon^{pl,U}$

$$\begin{aligned} \rho^{re}(0) &= \rho^o \left[\frac{\hat{\rho}}{\rho^o}(1 - D^U)^{2/\beta}\right]^{\frac{\varepsilon^{pl}}{\varepsilon^{pl,U}}} \\ \varepsilon^{pl,U} &= \varepsilon^U - \varepsilon^Y \end{aligned} \tag{5.35}$$

and, assuming perfect remodeling, at the end of remodeling processes (at time $t = t^f + T^f$)

$$\rho^{re}(t^f + T^f) = \rho^o \tag{5.36}$$

Remodeling processes consist of a unit resorption rate $\dot{v}^r$ that begins at time $t = t^r$ after loading, during which bone mass is removed by osteoclasts for a period of resorption T^r

$$\dot{v}^r = \dot{v}^r(\chi_i^r, t) \cdot [u(t - t^r) - u(t - [t^r + T^r])] \tag{5.37}$$

and a unit formation rate $\dot{v}^f$ that begins at time $t = t^f$ and lasts for a period of formation T^f, during which osteoid is deposited by osteoblasts and mineralizes into bone tissue

$$\dot{v}^f = \dot{v}^f(\chi_i^f, t) \cdot \left[u(t - t^f) - u(t - [t^f + T^f])\right] \tag{5.38}$$

where $u(t)$ is the Heaviside step function, and χ_i^r and χ_i^f are the biomechanical dependents of $\dot{v}^r$ and $\dot{v}^f$, respectively.

If all remodeling processes take place such that remodeling of the accumulated microdamage in V^m can be represented as the resorption of V^D and formation of V^{UD}, then in the control volume V

$$\begin{aligned} \dot{V} &= 0 \\ \dot{V}^D &= -V\dot{v}^r \\ \dot{V}^{UD} &= V\dot{v}^f \\ \dot{V}^m &= V(\dot{v}^f - \dot{v}^r) \\ \dot{V}^v &= V(\dot{v}^r - \dot{v}^f) \end{aligned} \tag{5.39}$$

The biological factors of χ_i^r and χ_i^f may include vascularity [76] or activation frequency, which is dependent on factors like age and hormone levels [4]. Biomechanical factors may include proximity to the periosteum and/or endosteum (Figure 1.1) and the effects of reoccurring local stress and/or strain. In this model, χ_i^r and χ_i^f are considered such that both $\dot{v}^r$ and $\dot{v}^f$ are dependent upon the micromechanical consistency of tissue and accumulated microdamage. As described in Section 1.2, a

BMU in cortical bone tunnels into and through bone tissue and creates new osteons, henceforth collectively called tunneling. A BMU in trabecular bone travels along a trabecula, digs into but not through its surface and deposits osteoid, henceforth collectively called digging.

The two bone tissues can be distinguished by the initial state h^o_{ij}, and so it is possible that BMU activity may be at least qualitatively predicted by h^o_{ij} as well. For example, a region of distinct osteons can be described by a high ρ^o and significantly directional $\hat{h}^o$. Knowing that a BMU travels along the longitudinal direction of osteons in a Haversian system, if $H^o_I \gg H^o_{II}, H^o_{III}$ then I is the longitudinal axis of the Haversian system (in more familiar mechanical terms, consider an apparent composite fiber direction of $\tilde{C}_{ijkl}$ in the cortex a long bone; see the Appendix). The cutting cone of a BMU is then be expected to travel along I and radially expand in $II - III$. Furthermore, in the timescale of cellular activity in a single resorption cavity, osteoblastic activity is then be expected to activate along I as a Heaviside function with respect to when osteoclastic activity previously occurred, and in $II - III$ as a function of the cement line radius (that is, the remodeling surface area of the cavity upon which osteoblastic activity occurs; see Figure 1.3).

The same may be true for trabecular tissue, at least from a probabilistic paradigm. Trabecular tissue can be described by a low ρ^o and less distinct directionality. Since a BMU travels along a trabecula, and since trabecular tissue is more fibrous than cortical tissue, the trajectory of a single BMU may not be predictable at the continuum level, but the average activity of a BMU population in a trabecular system might. For example, consider a trabecular system as a system of interconnected cylinders that are randomly oriented but statistically oriented such that their longitudinal axes tend to align with I. Examining any single trabecula, one may find it longitudinally oriented along II, in which case one would eventually observe a BMU traveling along II. But one would be more likely to find a trabecula longitudinally oriented along I, and this is described by $\hat{h}^o$.

If $\hat{h}^o$ describes the orientation of tissue and corresponding BMU activity, then ρ^o describes what cellular activity occurs. A notably high density then implies tunneling, while a notably low density implies digging. Both activities have distinct consequences when considering the transient effects of remodeling processes at the cellular level and their corresponding macroscopic phenomena. For example, consider a cross-section A with a void area A^r of a beam of stiffness E according to beam theory. For a given load, by the parallel axis theorem the area moment of inertia I decreases with increasing distance from the centroid of A^r to the centroid of A. So for a constant E, the flexural rigidity EI of the beam decreases in the plane of A with a more remote A^r, and this characterizes the individual effects of digging and tunnel: tunneling may be described as A^r in A, whereas digging may be described as A^r protruding into A from its boundary.

At the continuum level, let

$$n^{re}(t) = \int_0^t (\dot{v}^r - \dot{v}^f) d\tau \tag{5.40}$$

If $V^D(0) = V^{D,o}$ is considered as an addition to V^v after osteoclastic activity but before osteoblastic activity, then (5.40) is subject to the boundary conditions

$$n^{re}(t) = \begin{cases} 1 - (1 - D^L)^{2/\beta} & 0 \leq t \leq t^r \\ 1 - (1 - D^L)^{2/\beta} + \frac{V^{D,o}}{V} & t^r + T^r \leq t \leq t^f \\ n^o & t \to t^f + T^f \end{cases} \tag{5.41}$$

During resorption and formation, $\dot{v}^r$ and $\dot{v}^f$ are dependent upon the resorption surface area of the microstructural system. Since tunneling and digging occur in different bone systems, let

$$\dot{v}^r = \begin{cases} \dot{v}^{r,H} & \rho \geq \rho^H \\ \dot{v}^{r,T} & \rho < \rho^H \end{cases} \tag{5.42}$$

and

$$\dot{v}^f = \begin{cases} \dot{v}^{f,H} & \rho \geq \rho^H \\ \dot{v}^{f,T} & \rho < \rho^H \end{cases} \tag{5.43}$$

where ρ^H is a threshold density that signifies the distinction between the Haversian and trabecular systems H and T, respectively.

5.1.7 Determination of Remodeling Rates by Micromechanical Analysis

From (5.41)

$$\frac{V^{D,o}}{V} = n^{re}(t^f) - n^{re}(0) \tag{5.44}$$

If the porosity of the initial state of a Haversian system can be considered as consisting of a Haversian canal density N^H of average Haversian canal volume η^H, and the porosity of the reduced effective state $n^{re}(t)$ as consisting of the sum of N^H of volume η^H and the density of resorption cavities N^c of average volume $\eta(t)$, where considering the average fully resorbed cavity volume η^c

$$\eta(t) = \begin{cases} \eta^H & 0 \le t \le t^r \\ \eta^c & t^r + T^r \le t \le t^f \\ \eta^H & t \ge t^f + T^f \end{cases} \tag{5.45}$$

then the void volume in the Haversian system $V^{v,H}$ is subject to the boundary conditions

$$V^{v,H}(t) = V \begin{cases} (N^H + N^c)\eta^H & 0 \le t \le t^r \\ N^H\eta^H + N^c\eta^c & t^r + T^r \le t \le t^f \\ N^H\eta^H & t \ge t^f + T^f \end{cases} \tag{5.46}$$

(5.41) and (5.46) are satisfied in the form

$$\frac{V^{v,H}(t)}{V} = n^o + N^c \begin{cases} \eta(t) & t^r \le t \le t^r + T^r \\ \eta^c \left(1 - \frac{\eta^c - \eta(t)}{\eta^c - \eta^H}\right) & t^f \le t \le t^f + T^f \end{cases} \tag{5.47}$$

when then initial damaged volume in the Harversian system $V^{D,H}(0)$ is

$$\frac{V^{D,H}(0)}{V} = (n^{re}(0) - n^o)\left(\frac{\eta^c}{\eta^H} - 1\right) \tag{5.48}$$

So from (5.39), (5.42), (5.43) and (5.47)

$$\dot{v}^{r,H} = (n^{re}(0) - n^o)\frac{\dot{\eta}}{\eta^H}; \dot{\eta} \geq 0 \tag{5.49}$$

and

$$\dot{v}^{f,H} = -(n^{re}(0) - n^o)\left(\frac{\eta^c}{\eta^H}\right)\frac{\dot{\eta}}{\eta^c - \eta^H}; \dot{\eta} \leq 0 \tag{5.50}$$

Similarly, if the volume fraction of mass of the initial state of a trabecular system can be considered as consisting of the density of trabeculae N^T of average trabecula volume ζ^T, and the volume fraction of mass of the reduced effective state as consisting of the sum of N^T of volume ζ^T and the density of remodeled trabeculae N^r of average resorbed volume $\zeta(t)$, where considering the fully resorbed volume per remodeled trabecula ζ^r

$$\zeta(t) = \begin{cases} 0 & 0 \leq t \leq t^r \\ \zeta^r & t^r + T^r \leq t \leq t^f \\ 0 & t \geq t^f + T^f \end{cases} \tag{5.51}$$

then the void volume in the trabecular system $V^{v,T}$ is subject to the boundary conditions

$$V^{v,T} = V\begin{cases} 1 - (N^T\zeta^T - N^r\left(\zeta^T - \zeta^r\right)) & 0 \leq t \leq t^r \\ 1 - (N^T - N^r)\zeta^T & t^r + T^r \leq t \leq t^f \\ 1 - N^T\zeta^T & t \geq t^f + T^f \end{cases} \tag{5.52}$$

(5.52) and (5.41) are satisfied in the form

$$\frac{V^{v,T}(t)}{V} = n^o + N^r\begin{cases} \zeta^T - \zeta^r + \zeta(t) & t^r \leq t \leq t^r + T^r \\ \frac{\zeta^T}{\zeta^r}\zeta(t) & t^f \leq t \leq t^f + T^f \end{cases} \tag{5.53}$$

when the initial damaged volume in the trabecular system $V^{D,T}(0)$ is

$$\frac{V^{D,T}(0)}{V} = (n^{re}(0) - n^o)\frac{\zeta^r}{\zeta^T - \zeta^r} \tag{5.54}$$

So from (5.39), (5.42), (5.43) and (5.53)

$$\dot{v}^{r,T} = \frac{n^{re}(0) - n^o}{\zeta^T - \zeta^r}\dot{\zeta}; \dot{\zeta} \geq 0 \tag{5.55}$$

and

$$\dot{v}^{f,T} = -\left(\frac{n^{re}(0) - n^o}{\zeta^T - \zeta^r}\right)\left(\frac{\zeta^T}{\zeta^r}\right)\dot{\zeta}; \dot{\zeta} \leq 0 \tag{5.56}$$

5.1.8 Multiscale Description of Mechanical Failure

Let mechanical failure be described by the scenario in which no more initial volume of mass in V can be allocated to V^D during loading (that is, $V^{D,o} = V^{D,U}$) where from (5.33)

$$V^{D,U} = V(1 - n^o) \tag{5.57}$$

Considering the ultimate scalar damage in the Haversian and trabecular systems $D^{U,H}$ and $D^{U,T}$, respectively,

$$D^U = \begin{cases} D^{U,H} & \rho \geq \rho^H \\ D^{U,T} & \rho < \rho^H \end{cases} \tag{5.58}$$

where, from (5.34), (5.48), (5.57) and (5.58),

$$D^{U,H} = 1 - (1 - D^o)\left(1 - \frac{\eta^H}{\eta^c - \eta^H}\right)^{\beta/2} \tag{5.59}$$

and, from (5.34), (5.54), (5.57) and (5.58),

$$D^{U,T} = 1 - (1 - D^o)\left(2 - \frac{\zeta^T}{\zeta^r}\right)^{\beta/2} \tag{5.60}$$

5.2 Materials and Methods

5.2.1 Description of Model

A 1 x 1 meter linear cube element was tested in three dimensions under displacement loading. The element was fixed in the x direction at the face along the $y - z$ plane, in the y direction at the face along the $x - z$ plane and in the z direction along the $x - y$ plane. Displacement loading was applied at the second vertical face in the negative x direction, from no displacement to a specified ultimate strain. All results are reported such that compressive stress and strain are positive in the x direction.

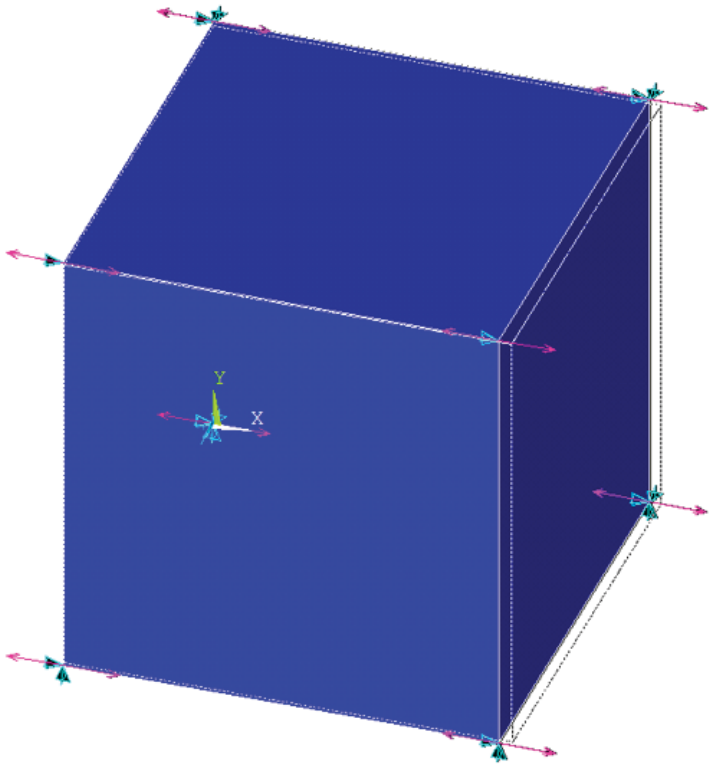

Figure 5.1. Unit element experimental setup for verification and testing of novel material model numerical implementation.

Material axes were such that the I, II and III material axes were aligned with the x, y and z directions, respectively (Figure 5.1). Experiments were performed in ANSYS v15.0 on a personal computer, Intel i7 4790K 4.00 GHz, 16.0 GB RAM. The proposed material model was implemented in Fortran77 according to the Usermat functionality provided by ANSYS, Inc. Numerical implentation of plastic deformation was formulated using the radial return algorithm [77]. Library files were compiled and linked in iFort 12.0 under the Intel academic software license.

Remodeling processes were then simulated for a set of final plastic strain results in each tissue. The timescale was such that loading occurred on day 0, after which no mechanical stimuli were applied. A ten day lag time was incorporated to account for lag time [1]. Equivalent plastic strain was applied for five trials in each tissue at the intervals of 500, 1,000, 2,000, 3,000 and 5,000 μ. Results of interest were recorded to

observe the evolution of anisotropy in tissue, as well as the results of the traditional definition of mechanical damage D^{mech} in the loading direction I

$$D^{mech} = 1 - \frac{E_I^t}{E_I^{t,o}}$$

where E_I^t and $E_I^{t,o}$ are the tangent modulii along I during and before loading, respectively. E_I^t was calculated from the axial stress σ_I and total strain component ε_I according to the Generalized Hooke's Law

$$E_I^t = \frac{\sigma_I}{\varepsilon_I}$$

5.2.2 Material Properties

From the description of resorption activity, all micromechanical descriptions of resorption were modeled as linear. Formation in trabecular bone was modeled as linear [78]. Formation in cortical bone was modeled according to [79] with respect to the cavity radius $R(t)$ and length l^H, such that

$$\eta(t) = \pi l^H (R(t))^2; t^f \leq t \leq t^f + T^f$$

where for the resorption cavity radius R^c and Haversian canal radius R^H

$$R(t) = R^c \left(\frac{R^H}{R^c} \right)^{\frac{t-t^f}{T^f}}$$

The final resorption volume in trabecular bone ζ^r was approximated so that $D^{U,T} \to 1$. ζ^T was approximated as a cylinder of trabecula diameter $2R^T$ and length $l^T = 20R^T$. For the material constants B and β in (5.1), the values of 1.76 GPa/(g/cc) and 3.2 were used, respectively [72]. Yield and ultimate strains for bone were 3,000 μ and 25,000 μ, respectively [9], and the ultimate strain for trabecular bone was doubled to model ductility. The parameter sets were such that, for (1) cortical bone: E_I = 16.6 GPa, $E_{II} = E_{III}$ = 12.5 GPa; and (2) trabecular bone: E_I = 1.39 GPa, $E_{II} = E_{III}$ = 1.20 GPa. All other micromechanical parameters were taken from [1] (Table 5.1).

Table 5.1. Material parameters of the novel material model experiments.

Parameter	Symbol		Value
Ideal bone density	$\hat{\rho}$		2.1 g/cc
Haversian canal diameter	$2R^H$		50 μm
Resorption cavity diameter	$2R^c$		200 μm
Haversian canal length	l^H		300 μm
Trabecula diameter	$2R^T$		200 μm
Trabecula length	l^T		2 mm
Resorption start time	t^r		3 days
Formation start time	t^f		43 days
Period of resorption	T^r		30 days
Period of formation	T^f		90 days
		Cortical bone	*Trabecular bone*
Initial apparent density	ρ^o	1.9 g/cc	0.9 g/cc
Yield strain	ε^Y	3,000 μ	3,000 μ
Ultimate strain	ε^U	25,000 μ	50,000 μ
Ultimate scalar damage	D^U	0.237	0.960
Fabric tensor - first principal value	$\hat{h}_I$	1.100	1.050
Fabric tensor - second principal value	$\hat{h}_{II}$	0.953	0.976
Fabric tensor - third principal value	$\hat{h}_{III}$	0.953	0.976

5.3 Results and Discussion

Numerical implementation of the proposed material model was verified by recording the von-Mises yield stress and ultimate scalar damage of both tissues during the experiment. Results were compared to the material parameters from Table 5.1. For the cortical bone experiment, all results fell within an acceptable range of the expected values, with a largest error of -2.43% for the ultimate scalar damage. For trabecular bone, errors were significantly higher, with the largest error recorded at

Table 5.2. Verification results of numerical implementation of the novel material model.

	Cortical		Trabecular	
Result	*Value*	*% Error*	*Value*	*% Error*
Yield stress	41.25 MPa	$7.49 \cdot 10^{-6}$	3.78 MPa	$3.46 \cdot 10^{-7}$
Ultimate scalar damage	0.231	-2.43	0.856	-11.0

-11.0% for the ultimate scalar damage. Greater error was partially attributed to the larger range of loading strain that was applied to trabecular bone. It was also assumed that, since trabecular bone was modeled as being more ductile, a larger degree of anisotropic evolution contributes to more significant errors that are inherent in nonlinear approximations (Table 5.2).

5.3.1 Macroscale Processes

Figure 5.2 shows the stress and strain results of the unit element experiment in cortical bone in the $I - II$ plane over the full strain range. After the elastic response, during which the stress response was linear, material softening was demonstrated by the negative correlation between stress and strain, which implies a decreasing E_I. The brittle nature of cortical bone was also observable by comparing the stress values at $\varepsilon = \varepsilon^Y$ and $\varepsilon = \varepsilon^U$, where a 6.7% decrease in stress was recorded from the onset of yielding to failure (ultimate von-Mises stress of 38.5 MPa). Results demonstrated the occurrence of plastic strain in the II and III directions to such an extent that the elastic strain in the II and III directions marginally decreased during plastic deformation. Consistently with experimental observation [49], the I plastic strain component was linear with respect to the total loading strain. All other strain components were nearly linear during elastic and plastic deformation.

Figure 5.3 shows the response of the reduced effective density and scalar and mechanical damage parameters of cortical bone as a function of the equivalent plastic

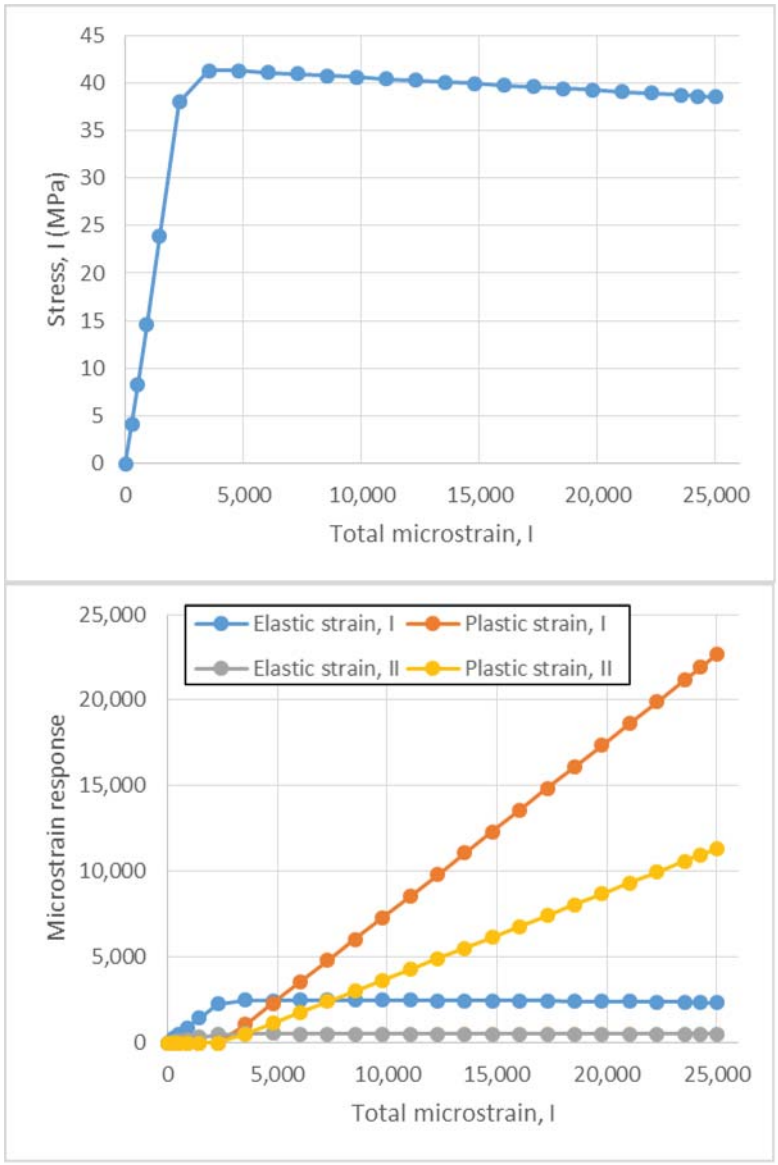

Figure 5.2. Axial stress and strain results vs. total loading strain in cortical bone in the novel material model unit element experiment.

strain. Both damage parameters were observed to increase with increasing plastic strain, while the density slightly decreased. The brittle nature of cortical bone was demonstrated by the nearly 23% scalar damage at the ultimate strain, where at fracture a sudden change of state was predicted, from significantly load bearing to failure. The mechanical damage curve was generally consistent with experimental

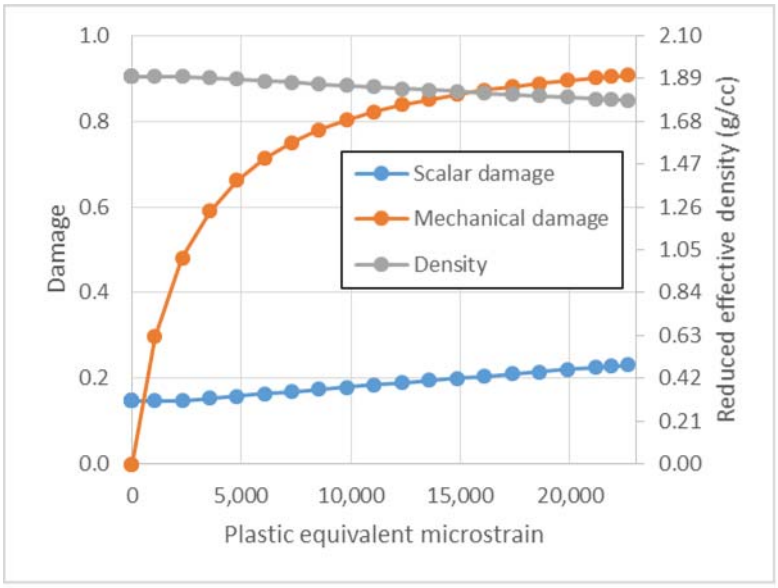

Figure 5.3. Damage parameters and reduced effective density of cortical bone vs. equivalent plastic strain during the novel material model unit element experiment.

data [49], where the only observed differences were related to the selected material parameters. This is significant because the proposed material model was used to model the description of bone that may have come from a different anatomical region than the region of those used in the experiments in [49]. Since the proposed material model is parameterized according to post-yield material parameters, it may then be useful to model not only the cortical bone used in [49], but cortical bone in various anatomical regions that respond similarly to mechanical stimulus.

Figure 5.4 shows the calculated Young's modulii of cortical bone in the $I-II$ plane, according to [72]. Both material parameters were calculated by recording the state variables h_{ij} during loading. The final state was calculated at the ultimate loading strain. In both states, the orthotropic nature of cortical bone was demonstrated, where before loading tissue was stiffest along the I direction, and after loading it was most compliant. Of interest is the effects of axial loading in the transverse plane, where stiffness was also reduced but to a lesser degree. Since plastic deformation

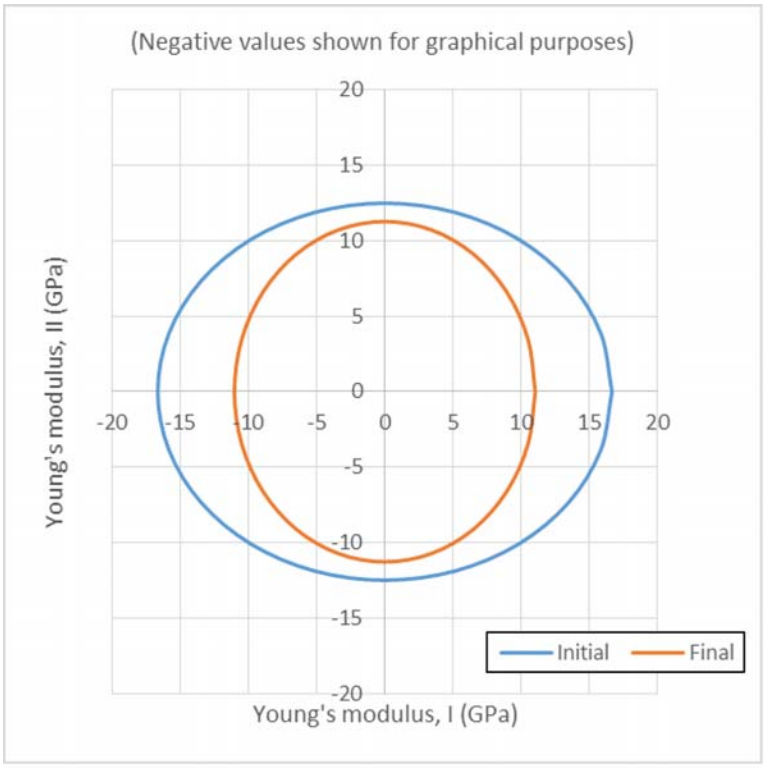

Figure 5.4. Material model Young's modulii in the $I-II$ plane before loading and at failure in cortical bone during the novel material model unit element experiment.

accompanies cracks, predictions from the proposed model may be useful for describing the initiation and propagation of microcracks along the osteons of a Haversian system, where microcracks tend to propagate along the lamellar interface [1]. In this case, the experiment from the proposed model for cortical bone may describe the initiation and propagation of microcracks at the Haversian canals and their redirection. As the loading strain continues towards failure, the reduction of stiffness in the transverse plane would result as a consequence of increased crack density in the interstitial bone around intact osteons.

Figure 5.5 shows the stress and strain results of the unit element experiment in trabecular bone in the $I-II$ plane over the full strain range. Similarly to results from cortical bone, results demonstrated a linear elastic response and material softening

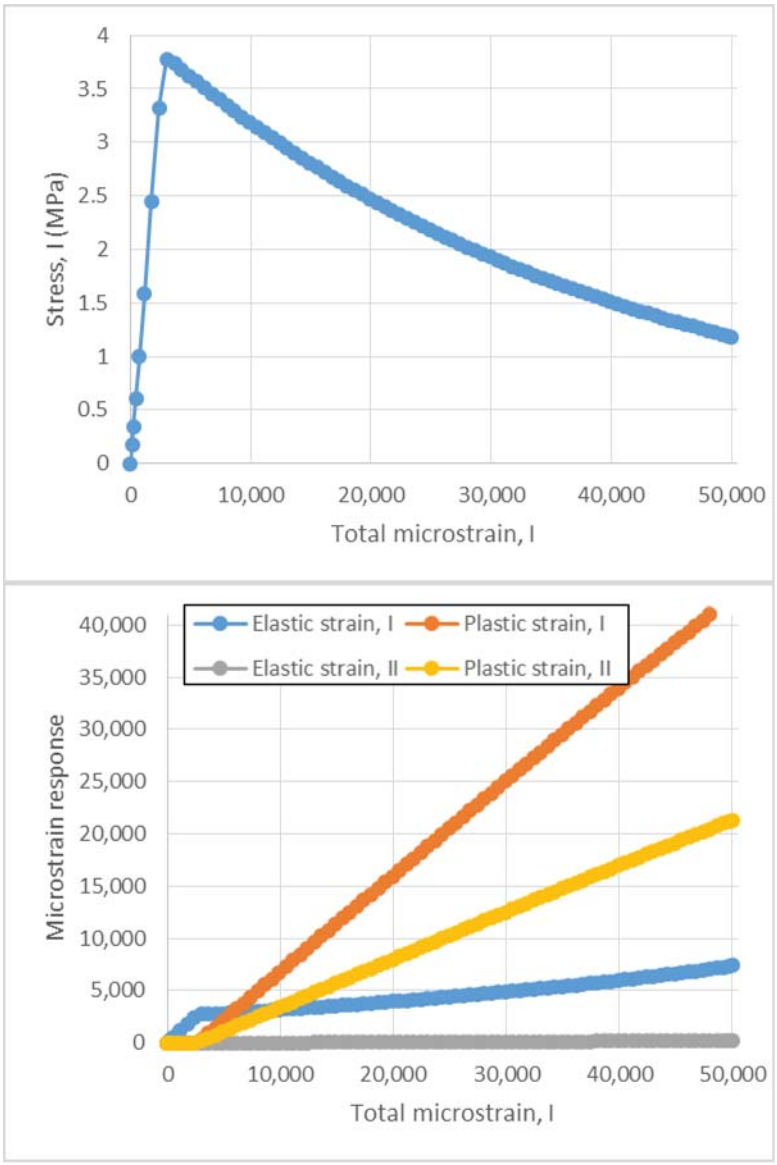

Figure 5.5. Axial stress and strain results vs. total loading strain in trabecular bone during the novel material model unit element experiment.

during plastic deformation, though for trabecular bone the stress-strain curve was more apparently nonlinear. Results showed a significantly more ductile behavior compared to cortical bone, where the von-Mises stress at failure was measured 1.18 MPa, respectively (69% decrease). Like cortical bone, the plastic strain components

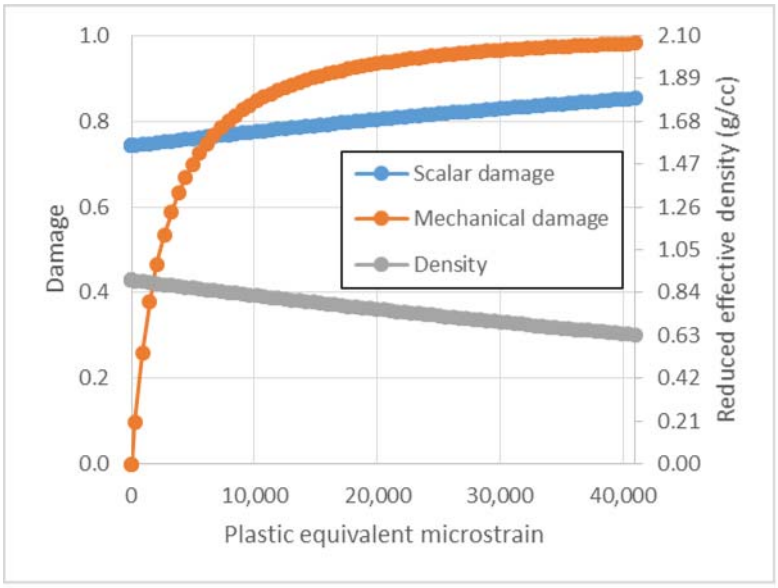

Figure 5.6. Damage parameters and reduced effective density of trabecular bone vs. equivalent plastic strain during the novel material model unit element experiment.

for trabecular bone were also linear responses to total loading strain, though elastic strain responses were more nonlinear. Axial loading strain also exerted observable effects on the plastic strain response in the transverse plane.

Figure 5.6 shows the response of the reduced effective density and scalar and mechanical damage parameters of trabecular bone as a function of the equivalent plastic strain. The calculated mechanical damage curve was similar to that from cortical bone, but was more asymptotic and more closely approached complete damage ($D^{mech} \rightarrow 1$). Plastic strain was observed to have a more significant effect on scalar damage and density, implying that the proposed model predicts a positive correlation between yield stress and damage accumulation. Associating plastic strain with the accumulation of microcracks, the proposed model then predicts a negative correlation between yield stress and crack propagation. Results showed that the proposed model captures the relative ductility of trabecular bone in that, at the continuum level, a much less than drastic change of state was predicted at failure.

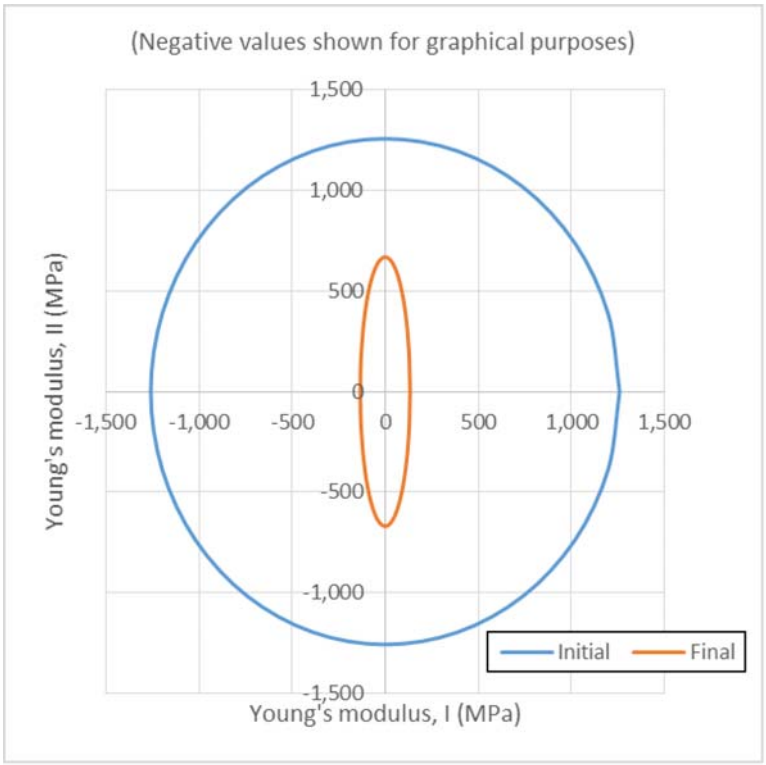

Figure 5.7. Material model Young's modulii in the $I-II$ plane before loading and at failure in trabecular bone during the novel material model unit element experiment.

Figure 5.7 shows the calculated Young's modulii of trabecular bone in the $I-II$ plane, according to [72]. Similarly to cortical bone, the final state was calculated at the ultimate loading strain, and the Young's modulii were calculated from the results of the state variables h_{ij}. Results showed the evolution of the nearly isotropic material state of trabecular bone to one of a clearly anisotropic nature. Compared to cortical bone, the proposed model predicted a more significant effect of axial loading in the transverse plane. In the microscale, the proposed model may represent the structural degradation of trabeculae that are oriented along I, with consequential effects in the $II-III$ plane.

5.3.2 Microscale Processes

Figure 5.8 shows the predicted immediate effects and resulting remodeling processes in cortical bone for five plastic loading cases. As expected, results showed a positive, linear correlation between the plastic strain and predicted density of resorption cavities. For the case of 500 μ plastic strain, the model predicted about two and a half resorption cavities per cubic millimeter, while for 5,000 μ the resorption cavity density was predicted to be approximately 24 cavities per cubic millimeter.

The effects of these during remodeling were then demonstrated by the varying degree of the reduced effective porosity after resorption, where higher plastic deformation caused greater reduction in apparent density as the cavities were resorbed (Figure 5.9). Since the experimental correlation from [49] showed a positive correlation between apparent density and stiffness, the proposed model predicts that after resorption but before formation cortical tissue will become more compliant, and increasingly so for higher plastic strains. Results then demonstrated the assumption

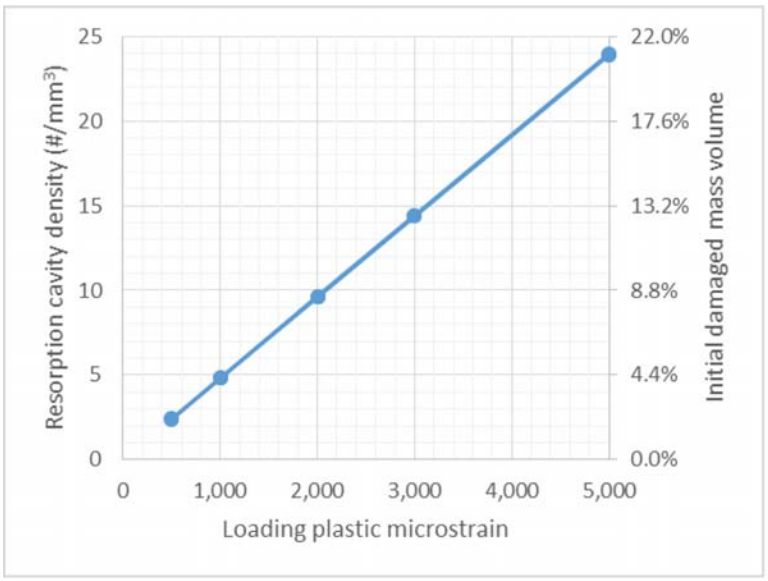

Figure 5.8. Predicted resorption cavity density and percent damaged volume in cortical bone vs. equivalent plastic strain during the novel material model micromechanics simulation.

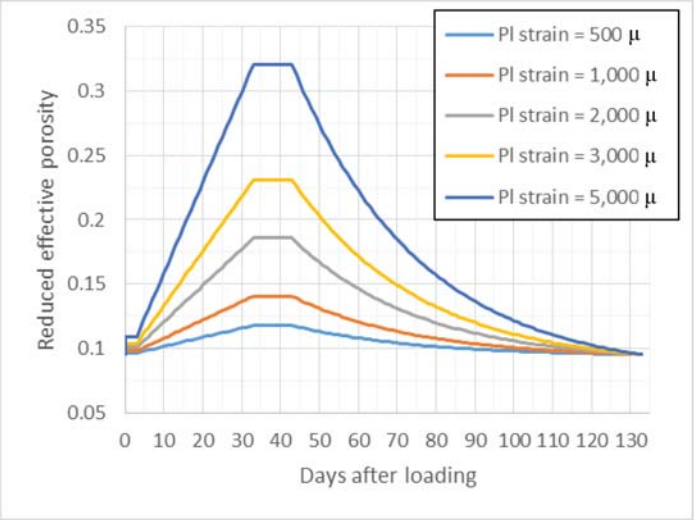

Figure 5.9. Reduced effective porosity in cortical bone vs. time during remodeling processes for five plastic loading cases during the novel material model micromechanics simulation.

of the proposed model that, for a single load case and uninterrupted remodeling processes, skeletal tissue will return to its former state.

Figure 5.10 shows the predicted immediate effects and resulting remodeling processes in trabecular bone for the same five plastic loading cases. Similarly to the cortical bone experiment, a positive, linear correlation was demonstrated between the plastic strain and predicted density of resorbed trabeculae. For the case of 500 μ plastic strain, the model predicted about 0.2 resorbed trabeculae per cubic millimeter, and about 2 remodeled trabeculae per cubic millimeter for 5,000 μ.

Figure 5.11 shows the predicted reduced effective porosity in trabecular bone during remodeling processes for the five load cases, where like in cortical bone greater reduction in apparent density was observed as a consequence of greater plastic deformation. Compared to cortical bone, any decrease in stiffness was predicted to be relatively less, where for the case of 5,000 μ an increase in porosity from resorption was measured at 193% and 12% in cortical and trabecular bone, respectively. For the case of 500 μ, an increase in reduced effective porosity from resorption was measured to be 22% in cortical bone and 1% in trabecular. Like in cortical bone, results demon-

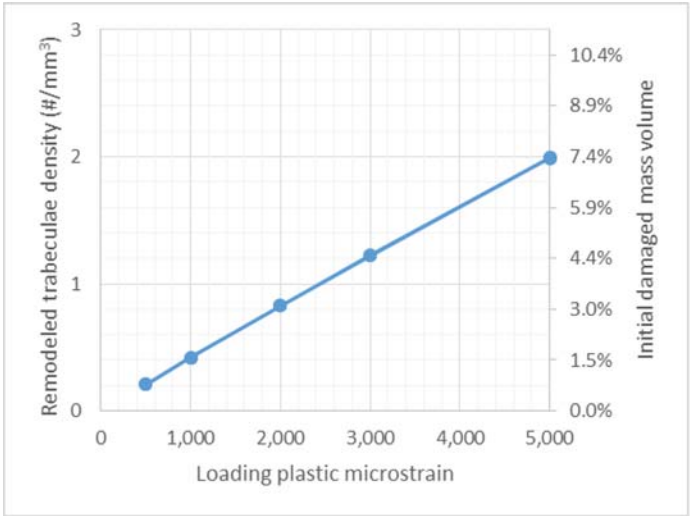

Figure 5.10. Predicted resorbed trabeculae density and percent damaged volume in trabecular bone vs. equivalent plastic strain during the novel material model micromechanics simulation.

strated the assumption of the proposed model that the state of tissue will return to its initial state before loading.

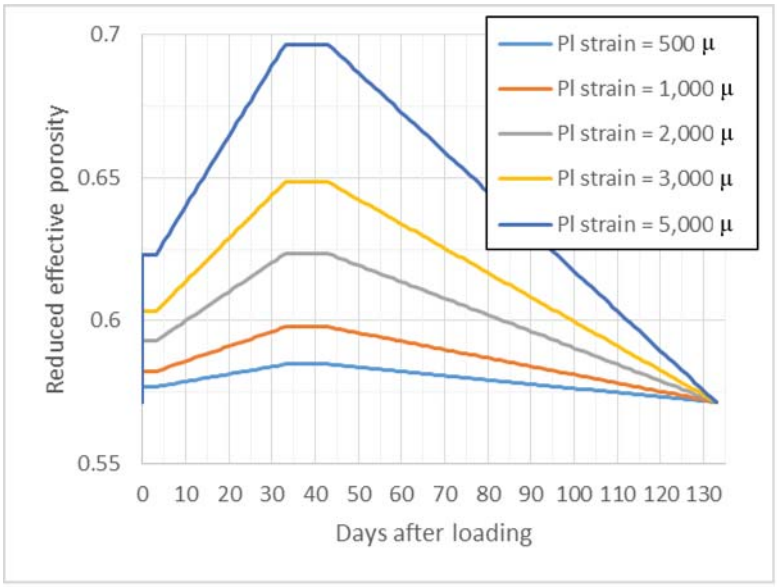

Figure 5.11. Reduced effective porosity in trabecular bone vs. time during remodeling processes for five plastic loading cases during the novel material model micromechanics simulation.

6. SUMMARY AND CONCLUSIONS

In this work, a finite element model was developed of a soft-tissue implant in a simplified crestal ridge according to literature. Nonlinear finite element analysis was performed to investigate the effects and significance of the crown-to-implant ratio, after investigating and scrutinizing the reliability of typical idealizations and methods of analysis in literature. Contributions were made in response to some determined limitations of the model, for the purpose of enhancing the reliability of applied finite element analysis in implant design.

In Chapter 2, significant disagreement between reported results of collected literature was investigated by adapting the finite element model to emulate reported models. Comparisons were made between finite element models and results from collected literature and those from the developed model, by mesh, maximum results and results distributions. A significant source of error was argued to be present in some literature as a result of material dissimilarity and the common idealization of osseointegration, which was deduced by correlating disagreement about results with reported details about mesh design. This idealization was speculated to cause mesh-dependency of results and the potential presence of a singular configuration at the implant interface.

In Chapter 3, the potential mesh-dependency of results in Chapter 2 was investigated by performing a convergence test at the interface of cortical bone and the implant. Experiments were performed for two materials sets, each with linear elastic material properties, and with the neglect and consideration of plastic deformation. 5% bilinear plastic hardening was implemented for the modeling of plastic deformation. In both sets, strain results diverged for all trials, confirming the mesh-dependency of results. The presence of a singularity in the typical implant FE model was argued, and the reliability of maximum results as a method of analysis in implant design

was challenged. Potential enhancements to mitigate the mesh-dependency of results were then proposed, including the statistical analysis of results distributions while also considering the geometric aspects of the mesh, and the modeling of material softening in skeletal tissue.

In Chapter 4, the crown-to-implant ratio of a soft-tissue implant under lateral loading was investigated by performing a 16-point design of experiments, considering orthotropic material properties, implant lengths of 6.0, 8.0, 10.0 and 12.0 mm and C/I ratios of 1.0, 1.5, 2.0 and 2.5. Comparing the results distributions of all trials, the significance of the C/I ratio was concluded to be secondary to other implant design considerations concerning strain concentrations. This conclusion was made by observing the occurrence of overloading strain in all trials, and the identification of sources of overloading strain for an implant length and crown height of 12 mm. A novel method of analysis and assessment of long-term stability was then presented and utilized. The proposed method calculated the average strain result and surface area of all contact element surfaces, and then allocated each contact surface area by predicted functional response to strain according to the Mechanostat hypothesis. The consistency of functional responses in skeletal tissue at the implant interface was then calculated by percent surface area, where inactivity, modeling and overloading were the primary predicted functional responses. Conclusions were made against short implants with high C/I ratios, where the shortest implant length configuration with a clinically advisable assessment was an implant length and crown height of 8 mm. An implant length and crown height of 6 mm was concluded to be volatile and requiring sufficient biological conditions for significant structural adaptation.

Chapter 5 presented a novel material model as a proposed improvement to mitigate the mesh-dependency discussed in Chapter 3. The model seeks to mathematically describe short-term damage accumulation in skeletal tissue according to experimental data, as well as consequential remodeling events. The model was derived from an existing mathematical description of the structural adaptation of skeletal tissue to repeated daily mechanical stimulus, which introduced a set of state variables that

describe both the porosity and quantitative directionality of tissue, as well as its biomechanical response to stress magnitude and frequency. In the proposed model, these state variables were related to plastic deformation from a single load case by proposing a novel material internal variable, called the scalar damage, and a virtual, reduced effective state, where the events of plastic deformation are influenced by the state of the material before loading. Information about the reduced effective state was then extended to the microscale, and a mathematical description of multiscale remodeling events was formulated. The scalar damage was then introduced to the microscale description to describe material failure. The model was numerically implemented, preliminary experiments of compressive loading were performed for descriptions of cortical and trabecular bone, and multiscale biomechanical observations were made. Results from the experiments demonstrated that the proposed model describes damage accumulation during plastic deformation consistently with experimental data.

6.1 Limitations

Results from the finite element model and their analysis are limited to the context of the modeling assumptions of the implant site. For the purpose of computational efficiency, the microscale topology of both skeletal tissues was neglected, and bone was modeled as homogeneous. Spatial variation of material properties in skeletal tissue was neglected for simplification and consistency with literature, though tissue is known to be more compliant in the neighborhood of an implant. Post-yield behavior in skeletal tissue was neglected due to the lack of consensus on material properties and modeling, even though the yield strain of bone is well within strain values observed in results. The implant interface was modeled with the idealizations of no relative motion between coincident parts, and no intermediary biological tissue.

As demonstrated in Chapter 3, results in cortical bone at the implant interface are dependent upon mesh resolution; this is particularly relevant for maximum results in

cortical bone, whether stress or strain. The mesh that was implemented in the design of experiments of Chapter 4 was experimentally observed to be of the finest resolution before the coalescence of results distributions became apparent, which was considered as an indication of significant model error. Though the novel method of analysis that was presented in Chapter 4 may mitigate the effects of divergent results to some extent, the choice in mesh resolution can still reasonably be called arbitrary when considering the certainty of some actual maximum result in cortical bone.

The reliability of the proposed novel method of analysis in Chapter 4 is inherently limited by a current lack of sufficient clinical data on the effects of the crown-to-implant ratio, with which the method should be reconciled and refined. Furthermore, assessments that were made of implant stability using this method were based on results from a single simulated load case, though implants experience a vast array of different and repeated load magnitudes, angles of attack and points of application *in vivo*. The proposed method of analysis generally neglects the influence of the number of times that a load is applied, and its application in Chapter 4 neglected the influence of axial load components according to the scope of the work. The method was implemented considering equivalent strain results as a generalization of all deviatoric strain components, which neglects the individual influence of tension and compression on biological response. The method was also applied to both cortical and trabecular bone, though cortical bone is primarily associated with implant stability.

Though the novel material model presented in Chapter 5 was generally consistent with experimental data concerning the post-yield behavior of cortical bone, the model contains a number of limitations due to insufficient experimental data and modeling assumptions. Firstly, the general hypothesis of the reduced effective virtual state assumes that after the initiation of softening the material continues to generally function as an undamaged material of a reduced density, and therefore of a reduced stiffness. This assumption neglects the consideration of the response of the material to immediate future load cases, within the time before the onset of remodeling activities. Even in reported results from the experimental work upon which the model was based [49],

the influence of immediate subsequent loading is apparent. Secondly, the material model describes the accumulation of damage while considering the anisotropic nature of bone. This description was shown to predict irreversible transverse deformation in response to purely axial loading, about which there is no corroborative or contradictory experimental data. Thirdly, the material model was based upon experimental work concerning cortical bone, and so the numerical experiments that were performed in Chapter 5 concerning the post-yield behavior of trabecular bone should be considered extrapolative. Fourthly, the description of remodeling events in each tissue, while utilizing some observed phenomena, was largely based upon qualitative descriptions of cellular activities that are still poorly understood. Modeling of these events was performed by applying information from the reduced effective virtual state to a homogenized description of cellular activities. While the validity of the proposed description of remodeling activities may be independent of the reduced effective virtual state, the description of remodeling activities was derived from the reduced effective virtual state, which, again, is hypothetical. Fifthly, the description of remodeling activities was derived based on the assumption that, if undisturbed, the material returns to its former state before the onset of loading damage, and so the model neglects the influence of damage from a single load case on long-term changes in the material state, as well as the influence of perturbations during and biological factors concerning remodeling processes.

6.2 Future Work

Concerning future research that may be related to or based on the work presented here, the most apparent final application of research is probably technologies that provide reliable, patient-specific predictions of the long-term stability of prostheses. This application is relevant both to dental implants and other prostheses placed elsewhere in the human body where, generally speaking, biologically foreign materials are integrated into the body and perform or provide various functions. Within the scope

of biomechanics, reliable predictions of implant stabiilty require a precise and total description of how tissue responds to and interacts with integrated foreign materials on multiple timescales.

Future work must be performed to augment the reliability of the finite element model of the implant site. Considering the continuum finite element model, some advanced contact model is required to more precisely describe the interactions between skeletal tissue and the implant at their interface. This contact model should then be implemented in finite element models of the implant site, where currently perfectly bonded contacts are typically utilized and were shown in this work to produce unreliable results. To develop this description, experimental work must first be performed to somehow isolate the interactions between skeletal tissue and various foreign materials of interest, from which the contact model should then be derived. This may be accomplished by press-fitting a cylindrical material of interest into a sample of skeletal tissue and measuring frictional forces during forced relative motion, or by some other experimental method. Until some contact model is developed and sufficiently supported, it is the author's opinion that greater attention should be given to the reliability of reported models, even to the reporting of some metric concerning convergence at or near the implant interface, which may at least provide better insight into disagreement among reported results in literature.

Regardless of the convergence of results from the continuum model, that some clinical data have implied a minimum crown-to-implant ratio suggests the need for a broader analysis of results from the finite element model when predicting implant stability than merely comparing maximum results to some threshold value. The proposed method of analysis in Chapter 4 introduces the consideration of the structural adaptation of skeletal tissue that, at least qualitatively, accounts for insufficient mechanical stimulus, which may be reflective of higher success rates for larger crown-to-implant ratios. With the consideration of sufficient clinical data on long-term success rates, and perhaps also with data on significant structural adaptation in response to implants, the proposed method should be refined to consider deformation

in tension and compression, as well as the significance of functional response in particular neighborhoods of the implant site. In Chapter 4 the method was generally applied to both skeletal tissues at the implant interface, without regard to the relative significance of structural adaptation in either tissue. In reality, reliable predictions according to the proposed method may be somewhat (even to entirely) unconcerned with trabecular bone, or perhaps only marginally concerned with results in trabecular bone at the thread features of the implant. An elaborate discussion of the specific limitations of the method would probably be mostly speculative, but a general (and perhaps excessively broad) hypothesis that seems apparent is that there is some set of temporospatially dependent weight functions that, when applied to the resulting strain distributions from some set of load cases, produces experimentally consistent predictions of long-term stability when considering structural adaptation.

Concerning the modeling of skeletal tissue, the novel material model in Chapter 5 presents a number of research opportunities, both in regards to the mechanical and biological aspects of the response of skeletal tissue to plastic deformation. While the effects of damage on stiffness in the direction of loading have been studied in cortical bone, its effects on the material properties of skeletal tissue in all material directions are poorly understood. The novel material model attempts to extend these experimental observations to all material directions by incorporating that bone is affected by shearing loads, which should be evaluated against future experimental work. The material model also describes remodeling activities with the assumption of no disturbances of cellular activities, and that the cellular activities of the remodeling process are directly related to the accumulation of damage from mechanical loading. The former assumption was implemented to describe the simplest imaginable case, and the latter was based on the elementary observations that sometimes bones are damaged, and yet somehow they continue to function. Exactly how these cellular activities are influenced by mechanical damage is poorly understood, particularly concerning individual microscopic phenomena and their interruption by external factors.

LIST OF REFERENCES

LIST OF REFERENCES

[1] R. B. Martin *et al.*, *Skeletal Tissue Mechanics*, 1st ed. New York: Springer-Verlag New York, Inc., 1998.

[2] W. E. Siri, "The gross composition of the body," in *Advances in Biological and Medical Physics*, L. John H and T. Cornelius A, Eds. Elsevier, 1956, vol. 4, pp. 239–280.

[3] F. H. Epstein *et al.*, "Bone marrow, cytokines, and bone remodeling - emerging insights into the pathophysiology of osteoporosis," *New England Journal of Medicine*, vol. 332, no. 5, pp. 305–311, 1995.

[4] H. M. Frost, "Wolff's law and bone's structural adaptations to mechanical usage: an overview for clinicians," *The Angle Orthodontist*, vol. 64, no. 3, pp. 175–188, 1994.

[5] W. Roux, "Der zuchtende kampf der teile, oder die teilauslese im organismus (theorie der'funktionellen anpassung')," *Wilhelm Engelmann, Leipzig*, vol. 2, 1881.

[6] J. C. Koch, "The laws of bone architecture," *American Journal of Anatomy*, vol. 21, no. 2, pp. 177–298, 1917.

[7] A. Goodship *et al.*, "Functional adaptation of bone to increased stress. an experimental study," *The Journal of Bone & Joint Surgery. American Volume*, vol. 61, no. 4, pp. 539–546, 1979.

[8] H. K. Uhthoff and Z. Jaworski, "Bone loss in response to long-term immobilisation," *The Journal of Bone & Joint Surgery*, vol. 60, no. 3, pp. 420–429, 1978.

[9] H. M. Frost, "Bone's mechanostat: A 2003 update," *The Anatomical Record Part A: Discoveries in Molecular, Cellular, and Evolutionary Biology*, vol. 275A, no. 2, pp. 1081–1101, 2003.

[10] J. Wolff, "The law of bone remodeling [translated from the 1892 original, das gesetz der transformation der knochen, by p. maquet and r. furlong]," 1986.

[11] J.-P. Geng *et al.*, "Application of finite element analysis in implant dentistry: A review of the literature," *The Journal of Prosthetic Dentistry*, vol. 85, no. 6, pp. 585–598, 2001.

[12] G. Limbert *et al.*, "Trabecular bone strains around a dental implant and associated micromotions-a micro-CT-based three-dimensional finite element study," *Journal of Biomechanics*, vol. 43, no. 7, pp. 1251–1261, 2010.

[13] A. Tovar *et al.*, "Topology optimization using a hybrid cellular automaton method with local control rules," *Journal of Mechanical Design*, vol. 128, no. 6, pp. 1205–1216, 2006.

[14] B. Şimşek *et al.*, "Effects of different inter-implant distances on the stress distribution around endosseous implants in posterior mandible: A 3d finite element analysis," *Medical Engineering & Physics*, vol. 28, no. 3, pp. 199–213, 2006.

[15] L. Baggi *et al.*, "The influence of implant diameter and length on stress distribution of osseointegrated implants related to crestal bone geometry: A three-dimensional finite element analysis," *The Journal of Prosthetic Dentistry*, vol. 100, no. 6, pp. 422–431, 2008.

[16] L. Kong *et al.*, "Selection of the implant thread pitch for optimal biomechanical properties: a three-dimensional finite element analysis," *Advances in Engineering Software*, vol. 40, no. 7, pp. 474–478, 2009.

[17] M. I. El-Anwar and M. M. El-Zawahry, "A three dimensional finite element study on dental implant design," *Journal of Genetic Engineering and Biotechnology*, vol. 9, no. 1, pp. 77–82, 2011.

[18] P. Ausiello *et al.*, "Effects of thread features in osseo-integrated titanium implants using a statistics-based finite element method," *Dental Materials*, vol. 28, no. 8, pp. 919–927, 2012.

[19] C.-L. Chang *et al.*, "Finite element analysis of the dental implant using a topology optimization method," *Medical Engineering & Physics*, vol. 34, no. 7, pp. 999–1008, 2012.

[20] S. L. D. de Moraes *et al.*, "A 3-d finite element study of the influence of crown-implant ratio on stress distribution," *Brazilian Dental Journal*, vol. 24, no. 6, pp. 635–641, 2013.

[21] I. C. Chou *et al.*, "Effects of implant neck design on primary stability and overload in a type iv mandibular bone," *International Journal for Numerical Methods in Biomedical Engineering*, vol. 30, no. 11, pp. 1223–1237, 2014.

[22] D. A. de Faria Almeida *et al.*, "Influence of tapered and external hexagon connections on bone stresses around tilted dental implants: three-dimensional finite element method with statistical analysis," *Journal of Periodontology*, vol. 85, no. 2, pp. 261–269, 2014.

[23] F. Ramos Verri *et al.*, "Biomechanical influence of crown-to-implant ratio on stress distribution over internal hexagon short implant: 3-d finite element analysis with statistical test," *Journal of Biomechanics*, vol. 48, no. 1, pp. 138–145, 2015.

[24] J. Nissan *et al.*, "The effect of crown/implant ratio and crown height space on stress distribution in unsplinted implant supporting restorations," *Journal of Oral and Maxillofacial Surgery*, vol. 69, no. 7, pp. 1934–1939, 2011.

[25] H. Shillingburg and J. Whitsett, *Fundamentals of fixed prosthodontics*, 3rd ed., ser. Quintessence, Chicago. Quintessence Publishing Co. Inc., 1997.

[26] R. J. Blanes *et al.*, "A 10 year prospective study of iti dental implants placed in the posterior region. ii: Influence of the crown-to-implant ratio and different prosthetic treatment modalities on crestal bone loss," *Clinical Oral Implants Research*, vol. 18, no. 6, pp. 707–714, 2007.

[27] R. J. Blanes, "To what extent does the crownimplant ratio affect the survival and complications of implant-supported reconstructions? a systematic review," *Clinical Oral Implants Research*, vol. 20, no. s4, pp. 67–72, 2009.

[28] G. Telleman *et al.*, "A systematic review of the prognosis of short (< 10 mm) dental implants placed in the partially edentulous patient," *Journal of Clinical Periodontology*, vol. 38, no. 7, pp. 667–676, 2011.

[29] B. S. Sotto-Maior *et al.*, "Influence of crown-to-implant ratio, retention system, restorative material, and occlusal loading on stress concentrations in single short implants," *The International Journal of Oral & Maxillofacial Implants*, vol. 27, no. 3, pp. e13–8, 2015.

[30] C. A. Duarte *et al.*, "Generalized finite element methods for three-dimensional structural mechanics problems," *Computers & Structures*, vol. 77, no. 2, pp. 215–232, 2000.

[31] L. Xu and S. Sengupta, "Dissimilar material joints with and without free-edge stress singularities: Part ii. an integrated numerical analysis," *Experimental Mechanics*, vol. 44, no. 6, pp. 616–621, 2004.

[32] R. J. Blanes *et al.*, "A 10 year prospective study of ITI dental implants placed in the posterior region. I: Clinical and radiographic results," *Clinical Oral Implants Research*, vol. 18, no. 6, pp. 699–706, 2007.

[33] N.-K. Lee and S.-H. Baek, "Effects of the diameter and shape of orthodontic mini-implants on microdamage to the cortical bone," *American Journal of Orthodontics and Dentofacial Orthopedics*, vol. 138, no. 1, pp. 8. e1–8. e8, 2010.

[34] J. Cha *et al.*, "Multiscale analyses of the bone-implant interface," *Journal of Dental Research*, vol. 94, no. 3, pp. 482–490, 2015.

[35] S. Basler *et al.*, "Towards validation of computational analyses of peri-implant displacements by means of experimentally obtained displacement maps," *Computer Methods in Biomechanics and Biomedical Engineering*, vol. 14, no. 02, pp. 165–174, 2011.

[36] P. Marcián *et al.*, "Finite element analysis of dental implant loading on atrophic and non-atrophic cancellous and cortical mandibular bone a feasibility study," *Journal of Biomechanics*, vol. 47, no. 16, pp. 3830–3836, 2014.

[37] J. A. Steiner *et al.*, "Computational analysis of primary implant stability in trabecular bone," *Journal of Biomechanics*, vol. 48, no. 5, pp. 807–815, 2015.

[38] C. Hellmich *et al.*, "Micromechanics-based conversion of CT data into anisotropic elasticity tensors, applied to FE simulations of a mandible," in *2008 MRS Fall Meeting, December 1, 2008 - December 5, 2008*, ser. Materials Research Society Symposium Proceedings, vol. 1152. Materials Research Society, 2008, Conference Proceedings, pp. 28–33.

[39] S.-H. Liao *et al.*, "Influence of anisotropy on peri-implant stress and strain in complete mandible model from CT," *Computerized Medical Imaging and Graphics*, vol. 32, no. 1, pp. 53–60, 2008.

[40] A. S. Bonnet *et al.*, "Biomechanical study of mandible bone supporting a four-implant retained bridge. finite element analysis of the influence of bone anisotropy and foodstuff position," *Medical Engineering & Physics*, vol. 31, no. 7, pp. 806–815, 2009.

[41] L. Borchers and P. Reichart, "Three-dimensional stress distribution around a dental implant at different stages of interface development," *Journal of Dental Research*, vol. 62, no. 2, pp. 155–159, 1983.

[42] J. M. Reina *et al.*, "Numerical estimation of bone density and elastic constants distribution in a human mandible," *Journal of Biomechanics*, vol. 40, no. 4, pp. 828–836, 2007.

[43] J. Martinez-Reina *et al.*, "A bone remodelling model including the directional activity of bmus," *Biomechanics and Modeling in Mechanobiology*, vol. 8, no. 2, pp. 111–127, 2009.

[44] N. Sykaras *et al.*, "Implant materials, designs, and surface topographies: their effect on osseointegration. a literature review," *International Journal of Oral & Maxillofacial Implants*, vol. 15, no. 5, 2000.

[45] E. Teixeira *et al.*, "A comparative evaluation of mandibular finite element models with different lengths and elements for implant biomechanics," *Journal of Oral Rehabilitation*, vol. 25, no. 4, pp. 299–303, 1998.

[46] M. Fondrk *et al.*, "Some viscoplastic characteristics of bovine and human cortical bone," *Journal of Biomechanics*, vol. 21, no. 8, pp. 623–630, 1988.

[47] I. Goda and J.-F. Ganghoffer, "3d plastic collapse and brittle fracture surface models of trabecular bone from asymptotic homogenization method," *International Journal of Engineering Science*, vol. 87, pp. 58–82, 2015.

[48] H. Isaksson *et al.*, "Precision of nanoindentation protocols for measurement of viscoelasticity in cortical and trabecular bone," *Journal of Biomechanics*, vol. 43, no. 12, pp. 2410–2417, 2010.

[49] H. Leng *et al.*, "Progressive post-yield behavior of human cortical bone in compression for middle-aged and elderly groups," *Journal of Biomechanics*, vol. 42, no. 4, pp. 491–497, 2009.

[50] A. N. Natali *et al.*, "Constitutive modelling of inelastic behaviour of cortical bone," *Medical Engineering & Physics*, vol. 30, no. 7, pp. 905–912, 2008.

[51] T. M. Keaveny *et al.*, "Biomechanics of trabecular bone," *Annual Review of Biomedical Engineering*, vol. 3, no. 1, pp. 307–333, 2001.

[52] R. Huiskes and E. Chao, "A survey of finite element analysis in orthopedic biomechanics: the first decade," *Journal of Biomechanics*, vol. 16, no. 6, pp. 385–409, 1983.

[53] N. Sharma *et al.*, "Finite element simulation of cortical bone under different loading and anisotropic yielding situations," in *Proceedings of the World Congress on Engineering and Computer Science*, vol. 2, 2012, Conference Proceedings.

[54] S.-H. Liao *et al.*, "Anisotropic finite element modeling for patient-specific mandible," *Computer Methods and Programs in Biomedicine*, vol. 88, no. 3, pp. 197–209, 2007.

[55] G. B. Sinclair, "Stress singularities in classical elasticity-I: Removal, interpretation, and analysis," *Applied Mechanics Reviews*, vol. 57, no. 1-6, pp. 251–297, 2004.

[56] D. B. Burr *et al.*, "Bone microdamage and skeletal fragility in osteoporotic and stress fractures," *Journal of Bone and Mineral Research*, vol. 12, no. 1, pp. 6–15, 1997.

[57] H. Frost, "Skeletal structural adaptations to mechanical usage (SATMU): 1. redefining wolff's law: the bone modeling problem," *The Anatomical Record*, vol. 226, no. 4, pp. 403–413, 1990.

[58] R. P. Heaney, "The natural history of vertebral osteoporosis. is low bone mass an epiphenomenon?" *Bone*, vol. 13, Supplement 2, pp. S23–S26, 1992.

[59] T. Sugiura *et al.*, "Evaluation of threshold stress for bone resorption around screws based on in vivo strain measurement of miniplate," *Journal of Musculoskeletal Neuronal Interactions*, vol. 1, no. 2, pp. 165–170, 2000.

[60] P.-O. J. Glantz and K. Nilner, "Biomechanical aspects of prosthetic implant-borne reconstructions," *Periodontology 2000*, vol. 17, no. 1, pp. 119–124, 1998.

[61] C. J. Goodacre *et al.*, "Clinical complications with implants and implant prostheses," *The Journal of Prosthetic Dentistry*, vol. 90, no. 2, pp. 121–132, 2003.

[62] F. Isidor, "Influence of forces on periimplant bone," *Clinical Oral Implants Research*, vol. 17, no. S2, pp. 8–18, 2006.

[63] Y.-T. Hsu *et al.*, "Biomechanical implant treatment complications: a systematic review of clinical studies of implants with at least 1 year of functional loading," *The International Journal of Oral & Maxillofacial Implants*, vol. 27, no. 4, pp. 894–904, 2011.

[64] H. Frost, "Bone mass and the mechanostat: a proposal," *The Anatomical Record*, vol. 219, no. 1, pp. 1–9, 1987.

[65] H. Roesler, "F. gaynor evans anniversary issue on bone biomechanics. the history of some fundamental concepts in bone biomechanics," *Journal of Biomechanics*, vol. 20, no. 11, pp. 1025–1034, 1987.

[66] C. Garaicoa-Pazmiño *et al.*, "Influence of crown/implant ratio on marginal bone loss: a systematic review," *Journal of Periodontology*, vol. 85, no. 9, pp. 1214–1221, 2014.

[67] L. Salguero *et al.*, "Micromechanical modeling of elastic properties of cortical bone accounting for anisotropy of dense tissue," *Journal of Biomechanics*, vol. 47, no. 13, pp. 3279–3287, 2014.

[68] H. Wiskott and U. C. Belser, "Lack of integration of smooth titanium surfaces: a working hypothesis based on strains generated in the surrounding bone," *Clinical Oral Implants Research*, vol. 10, no. 6, pp. 429–444, 1999.

[69] J. S. Hermann *et al.*, "Crestal bone changes around titanium implants. a radiographic evaluation of unloaded nonsubmerged and submerged implants in the canine mandible," *Journal of Periodontology*, vol. 68, no. 11, pp. 1117–1130, 1997.

[70] C. Fransson *et al.*, "Prevalence of subjects with progressive bone loss at implants," *Clinical Oral Implants Research*, vol. 16, no. 4, pp. 440–446, 2005.

[71] C. R. Jacobs, *Numerical simulation of bone adaptation to mechanical loading*. University Microfilms, 1996.

[72] M. Doblaré and J. M. García, "Anisotropic bone remodelling model based on a continuum damage-repair theory," *Journal of Biomechanics*, vol. 35, no. 1, pp. 1–17, 2002.

[73] J. Cordebois and F. Sidoroff, *Damage induced elastic anisotropy*. Springer, 1982, pp. 761–774.

[74] C. R. Jacobs *et al.*, "Adaptive bone remodeling incorporating simultaneous density and anisotropy considerations," *Journal of Biomechanics*, vol. 30, no. 6, pp. 603–613, 1997.

[75] H. H. Bayraktar *et al.*, "Comparison of the elastic and yield properties of human femoral trabecular and cortical bone tissue," *Journal of Biomechanics*, vol. 37, no. 1, pp. 27–35, 2004.

[76] R. Stewart *et al.*, "Increasing vascularity to improve healing of a segmental defect of the rat femur," *Journal of Orthopaedic Trauma*, vol. 25, no. 8, p. 472, 2011.

[77] R. Krieg and D. Krieg, "Accuracies of numerical solution methods for the elastic-perfectly plastic model," *Journal of Pressure Vessel Technology*, vol. 99, no. 4, pp. 510–515, 1977.

[78] R. Martin *et al.*, "Bone apposition rate differences in osteonal and trabecular bone," *Transactions of the Orthopaedic Research Society*, vol. 12, p. 178, 1987.

[79] J. Manson and N. Waters, "Observations on the rate of maturation of the cat osteon," *Journal of Anatomy*, vol. 99, no. Pt 3, p. 539, 1965.

APPENDIX

APPENDIX: ON THE REMODELING AND STIFFNESS TENSORS

According to [72], in the principal axes of the remodeling tensor, h_{ij} takes the form $\tilde{h}_{ij}$, where in three dimensions

$$\tilde{h}_{ij} = \begin{bmatrix} H_I & 0 & 0 \\ 0 & H_{II} & 0 \\ 0 & 0 & H_{III} \end{bmatrix} \tag{1}$$

where H_I, H_{II} and H_{III} are the principal values of h_{ij} ($H_I \geq H_{II} \geq H_{III} > 0$). The principal axes of h_{ij} are taken to be the material axes $\hat{n}_i$ that define the material coordinate system, where for the K^{th} principal value of h_{ij}

$$h_{ij}\hat{n}_j^{(K)} = H_{(K)}\hat{n}_i^{(K)} \tag{2}$$

The elasticity tensor in the principal axes of h_{ij}, $\tilde{C}_{ijkl} = \tilde{C}_{ijkl}(h_{ij})$, takes the Voigt form

$$\tilde{C}_{ijkl} = \left(\frac{1}{\hat{E}} \begin{bmatrix} \frac{1}{H_I^4} & -\frac{\hat{\nu}}{H_I^2 H_{II}^2} & -\frac{\hat{\nu}}{H_I^2 H_{III}^2} & 0 & 0 & 0 \\ & \frac{1}{H_{II}^4} & -\frac{\hat{\nu}}{H_{II}^2 H_{III}^2} & 0 & 0 & 0 \\ & & \frac{1}{H_{III}^4} & 0 & 0 & 0 \\ & & & \frac{1+\hat{\nu}}{H_{II}^2 H_{III}^2} & 0 & 0 \\ & sym & & & \frac{1+\hat{\nu}}{H_I^2 H_{III}^2} & 0 \\ & & & & & \frac{1+\hat{\nu}}{H_I^2 H_{II}^2} \end{bmatrix} \right)^{-1} \tag{3}$$

where $\hat{E}$ and $\hat{\nu}$ are experimentally determined material constants or piecewise parameters as functions of the apparent density ρ of a skeletal tissue of interest. If $\hat{E} = \hat{E}(\rho)$ and/or $\hat{\nu} = \hat{\nu}(\rho)$, then

$$\begin{aligned} \frac{\partial \hat{E}}{\partial \rho} &= 0 \\ \frac{\partial \hat{\nu}}{\partial \rho} &= 0 \end{aligned} \tag{4}$$